Mitochondrial stress-induced protein carboxyl-terminal alanine threonine tailing (msiCAT-tailing) facilitates glioblastoma tumorigenesis through the modulation of mitochondrial functions

Bei Zhang[1,†], Ting Cai[1,†], Esha Reddy[1], Yuanna Wu[1], Isha Mondal[2], Yinglu Tang[1], Adaeze Scholastical Gbufor[1], Jerry Wang[1,‡], Yawei Shen[3,4], Qing Liu[3,4], Raymond Sun[2], Winson S Ho[2], Rongze Olivia Lu[2,*], Zhihao Wu[1,*]

[1] Department of Biological Sciences, Dedman College of Humanities and Sciences, Southern Methodist University, Dallas, TX 75275, USA.

[2] Department of Neurological Surgery, University of California, San Francisco, CA 94143, USA.

[3] Department of Biological Sciences, Clemson University, Clemson, SC 29634, USA.

[4] Center for Human Genetics, Clemson University, Greenwood, SC 29646, USA.

[†] These authors contributed equally.

[‡] Current address: McCombs School of Business, University of Texas at Austin, Austin, TX 78712, USA

* Correspondence authors: Rongze Olivia Lu (rongze.lu@ucsf.edu); Zhihao Wu (zhihaowu@smu.edu)

Highlights

- Glioblastoma (GBM) cells have a disturbed RQC pathway
- msiCAT-tailing on ATP5α in GBM cells increases mitochondrial membrane potential
- This msiCAT-tailing prevents MPTP opening
- ATP5α msiCAT-tailing also inhibits drug-induced apoptosis in GBM cells
- Blocking msiCAT-tailing impedes the overall growth of GBM cells

Abstract

The rapid and sustained proliferation of cancer cells necessitates increased protein production, which, along with their disrupted metabolism, elevates the likelihood of translation errors. Ribosome-associated quality control (RQC), a recently identified mechanism, mitigates ribosome collisions resulting from frequent translation stalls. However, the precise pathophysiological role of the RQC pathway in oncogenesis remains ambiguous. Our research centered on the pathogenic implications of mitochondrial stress-induced protein carboxyl-terminal alanine and threonine tailing (msiCAT-tailing), a specific RQC response to translational arrest on the outer mitochondrial membrane, in glioblastoma (GBM). The presence of msiCAT-tailed mitochondrial proteins was observed commonly in glioblastoma stem cells (GSCs). Exogenous introduction of mitochondrial ATP synthase F1 subunit alpha (ATP5α) protein with artificial CAT-tail mimicking sequences enhanced mitochondrial membrane potential (ΔΨm) and inhibited mitochondrial permeability transition pore (MPTP) formation. These alterations in mitochondrial characteristics provided resistance to staurosporine (STS)-induced apoptosis in GBM cells. Consequently, msiCAT-tailing can foster cell survival and migration, whereas blocking msiCAT-tailing via genetic or pharmacological intervention can impede GBM cell overgrowth.

Key words

Glioblastoma (GBM); Ribosome-associated quality control (RQC); Mitochondrial stress-induced protein carboxyl-terminal alanine and threonine tailing (msiCAT-tailing); ATP synthase F1 subunit alpha (ATP5α); Mitochondrial membrane potential (MPP or ΔΨm); Mitochondrial permeability transition pore (MPTP); Apoptosis

Introduction

Proteins are vital to biological processes, and their overproduction is crucial for rapidly proliferating cells, like cancer cells. To cope with this increased demand, cancer cells extensively reform the initiation, elongation, and termination phases of their protein synthesis (1). However, heightened protein translation elevates the chance of errors (2). Coupled with metabolic perturbations such as energy fluctuations and redox imbalances, the capacity to address disruptions during translation becomes indispensable. Ribosome-associated quality control (RQC) is a recently discovered suite of rescue mechanisms in eukaryotes that detect and resolve stalled, decelerated, or collided ribosomes during translation elongation or termination (3, 4).

RQC is a multi-step process initiated by the ZNF598/RACK1 complex recognizing the distinctive 40S-40S interface on collided ribosomes, which triggers ubiquitination of specific 40S subunit proteins (5, 6). Subsequently, the ASC-1 complex separates the leading ribosome (7, 8). Following this, events that transpire include: ribosomal subunits dissociation and recycling (9), modification of the nascent peptide chains by C-terminal alanine and threonine addition (CAT-tailing) (10), release of CAT-tailed products from the 60S subunits by ANKZF1/VMS1 (11), and degradation of aberrant peptides by the Ltn1/VCP/NEMF complex (4). The functional significance of CAT-tailed proteins produced during RQC remains incompletely understood. They may facilitate Ltn1-mediated ubiquitination (12) and promote the degradation of defective nascent peptides by exposing lysine residues (13, 14). Nonetheless, they are also prone to forming detergent-insoluble aggregates (15, 16). Furthermore, contingent upon the nature of the original protein and its subcellular location, CAT-tailed proteins might possess specific, albeit currently unclear, functions. Notably, CAT-tailed proteins have been implicated in the pathogenesis of several neurodegenerative diseases, indicating a significant role in their

progression (17-19).

Cancerous cells demonstrate increased translation irregularities, including stop codon readthrough (20), frame-shifting (21), and oxidative stress-induced ribosomal arrest (22), suggesting a potential function for the RQC pathway. While CAT-tail modification on mitochondrial proteins due to compromised RQC has been noted in HeLa cells, the mechanistic involvement of RQC factors in cancer biology remains largely unexplored (17). Notably, the expression profile of various RQC factors (e.g., ASCC3, ABCE1, ANKZF1, and VCP) is dysregulated in cancer (23-26). Interestingly, RQC factors can display opposing functions in cancer development and suppression depending on specific circumstances, with some factors like ABCE1, ASCC3, and VCP suppressing cancer cell growth upon downregulation (23, 24, 26), while others like NEMF/Clbn and ZNF598 may promote it upon inhibition (27, 28). This indicates a nuanced, context-dependent role for RQC components in cancer cells, subject to both genetic and environmental modulators. A recent study examined ANKZF1's mechanism in mitochondrial proteostasis and its influence on glioblastoma multiforme (GBM) progression (29). However, this study employed a non-physiological mitochondria-targeted GFP to induce matrix proteotoxicity, leaving the role of endogenous mitochondrial proteins in this process ambiguous.

Mitochondrial stress leads to co-translational import anomalies, eliciting widespread CAT-tailing (mitochondrial stress-induced CAT-tail or msiCAT-tail) of nuclear-encoded mitochondrial proteins, including C-I30 (Complex-I 30 kDa subunit protein, NDUS3) (17, 30). The functional ramifications of these msiCAT-tailed proteins in mitochondrial biology remain poorly elucidated. Given that CAT-tailing imparts new properties to proteins, it may contribute to distinctive features of cancer cell mitochondria, such as hyperpolarization (31, 32) and resistance to drug-induced apoptosis linked to high mitochondrial membrane potential ($\Delta\Psi m$) (33-35). This

membrane potential across the inner membrane of mitochondria, essential for ATP production by OXPHOS, is sustained by the electron transport chain (Complexes I to IV), which pumps protons (H^+) into the intermembrane space (36), and ATP synthase (Complex V), which leverages this gradient (37). While numerous malignant cells exhibit reduced OXPHOS despite high energy demands (38), the mechanisms by which they maintain or elevate ΔΨm remain an unresolved question (31).

In this study, we investigated msiCAT-tailing modification on the mitochondrial ATP synthase F1 subunit alpha (ATP5α). We discerned that msiCAT-tailed ATP5α is present in GBM. The mimic short-tailed ATP5α (ATP5α-AT3 in subsequent studies) can integrate into the ATP synthase, leading to an augmented ΔΨm and attenuated mitochondrial permeability transition pore (MPTP) assembly and opening. Consequently, msiCAT-tailed ATP5α enhances GBM cell resistance to programmed cell death induced by staurosporine (STS) and temozolomide (TMZ), thereby fostering cancer cell survival, proliferation, and migration. Conversely, impeding msiCAT-tailing diminishes cancer cell growth and resensitizes GBM cells to apoptosis. Our findings underscore the involvement of CAT-tailed mitochondrial proteins in tumorigenesis and emphasize the significance of the RQC pathway in oncobiology. These outcomes suggest that components and products of the RQC pathway may offer promising therapeutic targets for GBM.

Results

Presence of msiCAT-tailed Proteins in Glioblastoma Cells

While dysregulation of individual ribosome-associated quality control (RQC) factors is documented across various cancers (e.g., adenocarcinoma, non-small cell lung, prostate, and colon carcinomas), a comprehensive analysis of the RQC pathway in glioblastoma (GBM) has been lacking (23-26). Our analysis of transcriptomic data from a cohort of 153 GBM patients and 206 healthy controls, sourced from public datasets, revealed significantly elevated expression (logFC (fold change) > 1; adj.P.Val < 0.001) of RQC pathway genes, such as *ABCE1*, *ASCC1-3*, *RACK1*, and *VCP*, in GBM cells(39). Conversely, *ANKZF1* was significantly downregulated (logFC = -0.43, adj.P.Val = 0.0005) (Fig. 1A, Table S1). The expression change in these genes implies RQC pathway activation and potential accumulation of CAT-tailed proteins in GBM. Mitochondrial stress-induced protein mitochondrial Complex-I 30 kDa (C-I 30, also known as NDUS3), an endogenous RQC substrate with msiCAT-tails, was previously identified in HeLa cells (17). Examination of patient-derived GBM stem cells (GSCs) and normal neural stem cells (NSCs) revealed that GSCs, unlike NSCs, exhibited several msiCAT-tailed mitochondrial proteins, including NDUS3, COX4 (Cytochrome c Oxidase subunit 4), and ATP5α (ATP synthase F1 subunit alpha). Consistent with the detection of these msiCAT-tailing signals, increased NEMF (Nuclear Export Mediator Factor) levels (10) and decreased ANKZF1 (Ankyrin Repeat and Zinc-finger Peptidyl tRNA Hydrolase 1) expression (11) were observed in patient-derived GSCs (Fig. 1B), further indicative of enhanced CAT-tailing activation, mirroring bioinformatics findings in GBM samples. A murine GBM model exhibited analogous RQC pathway alterations, with increased NEMF and decreased ANKZF1 expression in transplanted SB28 gliomas compared to normal brain tissue (Fig. S1A, B).

The subsequent experiments were conducted using two GBM cell lines, SF268 (SF in figures) (40) and GSC827 (GSC in figures) (41), and two control cell lines, SVG p12 (SVG in figures) and Normal Human Astrocytes E6/E7/hTERT (NHA in figures) (42). RQC protein expression analysis revealed decreased ANKZF1 and increased ABCE1, ASCC3, and NEMF expression in GSC827 and SF268 cells, consistent with findings in patient-derived GSCs (Fig. S1C). Intriguingly, induction of CAT-tailing on a Flag-tagged β-globin reporter via a non-stop protein translation system demonstrated significantly higher CAT-tailed protein (β-globin-nonstop) production in GBM cells (43). This process was inhibitable by the CAT-tailing elongation inhibitor anisomycin and NEMF knockdown (sgNEMF), but not cycloheximide treatment, as evidenced by a decreased ratio of CAT-tailed (Red) to non-CAT-tailed bands (Green) (Fig. 1C).

Next, to investigate the biological implications of CAT-tailing, artificial CAT-tails were introduced to mitochondrial proteins. Due to the variability in CAT-tailing, prior research simulated this process by adding alanine-threonine (AT) repeat tails to the C-terminus of mitochondrial proteins (17). According to recent studies, the chosen tail sequence can be stabilized by its high threonine content (44, 45). ATP5α, a highly abundant mitochondrial protein with roles in cancer, was selected to study the unique functions of CAT-tailed forms (46, 47). siATP5α knockdown first confirmed the upper band signal in GSCs as authentic ATP5α, demonstrated by its disappearance concurrent with the main band's weakening (Fig. S2A). Then, we confirmed that this upper band signal corresponded to changes in CAT-tailing, which could be effectively inhibited by NEMF knockdown and anisomycin treatment (Fig. S2B). Due to the indistinct nature of the endogenous msiCAT-tailed ATP5α signal, exogenously expressed Flag-ATP5α was utilized here.

To investigate the potential new function provided by CAT-tailed proteins, control (SVG and NHA) and GBM (SF268 and GSC827) cell lines overexpressed ATP5α with three (ATP5α-AT3) or twenty (ATP5α-AT20) AT repeats. Consistent with earlier findings, only the long-tailed ATP5α-AT20 exhibited post-translational modifications and detergent-resistant insoluble aggregates, appearing as slower migrating bands and a high molecular weight smear in protein electrophoresis (Fig. 1D). Based on comparing exogenously expressed (indicated by red boxes) to endogenous proteins (indicated by green boxes), GBM cell lines (GSC827, SF268) showed increased accumulation of ATP5α-AT20 compared to control cells (SVG, NHA). This accumulation may occur due to increased stability and reduced degradation of long-tailed proteins, a malfunctioning protein quality control system, enhanced cellular tolerance to protein accumulation, or a combination of these factors. Subcellular localization analysis showed that the short AT tail (AT3) did not significantly alter ATP5α's mitochondrial localization, similar to the tailless protein. However, a significant portion of ATP5α-AT20 was found in the cytoplasm near mitochondria, forming protein aggregates, with the highest proportion in highly malignant GSC cells (Fig. S2C, D). Notably, poly-glycine-serine tails (short, GS3, and long, GS20) did not induce insoluble protein aggregation or intracellular punctate distribution (Fig. S2E-G), highlighting the importance of specific amino acid composition.

Importantly, in GBM cells, both exogenous tailed proteins and the endogenous ATP5α formed clusters attached to the outer mitochondrial membrane (Fig. 1E, F). Similar aggregate formation in GBM cells was also observed with other mitochondrial proteins, such as NDUS3 (Fig. S3A, B). Furthermore, we examined the mouse GBM models. Akin to *in vitro* culture, ATP5α in transplanted SB28 glioma formed more punctate signals and did not always colocalize with the mitochondrial marker TOM20 (Fig. S3C-E). These findings collectively indicate a

disruption of the RQC pathway, leading to the presence of msiCAT-tailed proteins in GBM cells.

msiCAT-tailed ATP5α Elevates Mitochondrial Membrane Potential (ΔΨm)

Some cancer cells exhibit altered mitochondrial physiology, maintaining or increasing mitochondrial membrane potential (ΔΨm) despite reduced respiration. This was observed in patient-derived GSC cells, which demonstrated higher ΔΨm but lower ATP production than control NSC cells (Fig. 2A, B). Similarly, GBM cell lines, GSC827 and SF268, displayed comparable or higher ΔΨm and lower ATP levels relative to the control NHA cell line (42) (Fig. S4A-C). Genetic inhibition of msiCAT-tailing, via NEMF knockdown (sgNEMF) or ANZKF1 overexpression (oeANZKF1) (Fig. S4D), as well as pharmacological inhibition by anisomycin treatment, effectively reduced ΔΨm in GBM cells but not in NHA cells (Fig. 2C, D).

Our next investigation of msiCAT tail proteins revealed their impact on mitochondrial function. Expression of Flag-tagged ATP5□-AT3 and ATP5□-AT20 in GBM and control cell lines elevated ΔΨm specifically in GBM cells (Fig. 2E). Overexpression of ATP5□-GS3 and ATP5□-GS20 did not exhibit this effect (Fig. S4E). To our surprise, even with suppressed endogenous CAT-tailing through sgNEMF and oeANZKF1 in GSC cells, the introduced AT3 and AT20 proteins could still effectively elevate ΔΨm (Fig. 2F, G). This finding suggests that CAT-tailing of ATP5□ may be a significant contributor to the observed mitochondrial phenotype (Fig. 2G). Blue Native Polyacrylamide Gel Electrophoresis (BN-PAGE) illustrated distinct effects based on CAT-tail length. ATP5□-AT3 integrated into the mitochondrial respiratory chain complex, whereas ATP5□-AT20 formed high molecular weight complexes or remained as monomers (Fig. 2H). In mitochondrial physiological activity assays using the Agilent Cell

Mitochondrial Stress Test, the oxygen consumption rate (OCR) was directly measured to assess mitochondrial respiration. Our findings indicate that expressing both ATP5□-AT3 and ATP5□-AT20 negatively impacted mitochondrial oxidative phosphorylation. This impairment leads to a reduction in ATP synthesis, basal respiration, and maximal respiration rates (Fig. 2I-L). These data suggest that both short and long tails on ATP5□ proteins influence mitochondrial function, although potentially through different mechanisms. Short CAT-tails may directly act on ATP synthase function and thus affect the respiratory chain complex, while long CAT-tails form protein aggregates, causing mitochondrial proteostasis stress and thus indirectly affecting mitochondrial respiration (17, 29). This differential impact of CAT-tail length suggests a nuanced regulation of mitochondrial function mediated by ATP5□ modifications.

msiCAT-tailing Influences Mitochondrial Permeability Transition Pore (MPTP) Dynamics

Beyond its traditionally recognized role in ATP production, the F_1F_0 ATP synthase has garnered increasing attention as a potential structural component of the mitochondrial permeability transition pore (MPTP) complex (48-50). Given the possibility that CAT-tailed proteins like ATP5□ might modulate MPTP function, this investigation sought to elucidate the mechanism by which msiCAT-tailing modulates MPTP dynamics (open-close state). Comparative analyses conducted in GBM and control cells revealed that MPTP in GSC827 cells predominantly exists in a closed conformation, indicated by strong Calcein signals. Notably, the treatment of anisomycin, a pharmacological CAT-tailing inhibitor, effectively induced MPTP opening in GSC827 cells, as indicated by decreased Calcein signals (Fig. 3A, B). This effect was concomitant with the diminished aggregation of endogenous ATP5α (Fig. 3E, F). Furthermore, corroborative evidence was obtained through genetic manipulation. Specifically, genetic

inhibition of CAT-tailing via NEMF knockdown (sgNEMF) resulted in a similar decrease in Calcein signaling and a reduction in ATP5α accumulation (Fig. 3C, D, G, H), aligning with the results obtained using anisomycin. In contrast, treatment with cycloheximide, a general translation inhibitor, did not significantly alter Calcein or ATP5α aggregation signals (Fig. S5A-D), suggesting that non-specific translation inhibition does not impact the mitochondrial MPTP state. The crucial role of CAT-tail modifications on ATP5α in modulating MPTP status was further substantiated by the observation that overexpression of artificially synthesized AT repeat tails (AT3 and AT20) restored Calcein signals despite the inhibition of endogenous CAT-tailing (Fig. S5E).

The MPTP is recognized to participate in the transient efflux of protons, calcium ions (Ca^{2+}), and other signaling molecules from the mitochondrial matrix during brief opening episodes (51). To quantitatively evaluate the MPTP open/closed state, the mitochondrial Ca^{2+} Retention Capacity (CRC) assay was employed, which measures the amount of Ca^{2+} required to elicit MPTP opening. Our results revealed that GSC827 cells exhibited a greater CRC than NHA cells. Pre-treatment with anisomycin or knockdown of NEMF (sgNEMF) significantly decreased the CRC in GBM cells, indicating MPTP opening upon the loss of CAT-tailed proteins (Fig. 3I, J). Consistent with Calcein staining results (Fig. S5A, B), cycloheximide treatment did not substantially alter CRC measurements (Fig. S6A, B). Conversely, enhancing CAT-tailing (e.g., via oeNEMF and siANKZF1) led to an increase in CRC (Fig. S6A, B), although this effect was less pronounced in GSCs, potentially due to their inherently active CAT-tailing and closed MPTP.

To further investigate the impact of specific AT repeat tails on MPTP opening, artificial AT repeat tails on ATP5α were introduced into GBM cells. It was found that the short AT tail (AT3) inhibited MPTP opening, while the long AT tail (AT20) displayed a weaker effect (Fig. 3K,

L), potentially due to their different integration into ATP synthase (Fig. 2G). Complex co-immunoprecipitation assay did not detect direct interactions between ATP5□ with AT3 or AT20 tails and MPTP components Cyclophilin D (Cyp-D) and adenine nucleotide translocator 2 (ANT2) (Fig. S6C). However, Cyp-D expression was reduced upon ectopic expression of ATP5□-AT3 and ATP5□-AT20, suggesting decreased MPTP formation (Fig. S6D). Intriguingly, BN-PAGE analysis revealed that both ATP5□-AT3 and ATP5□-AT20 altered ANT1/2-containing complexes, with expected bands disappearing (indicated by *) and aggregates forming (at the top), supporting the notion that ATP synthase is integrated into the MPTP supercomplex due to the spatial proximity of the ANT1/2 complex and ATP synthase (Fig. 3M). In conclusion, msiCAT-tailed ATP5□ proteins, particularly those with short AT3 tails, are integrated into ATP synthase and have a substantial influence on modulating MPTP status.

msiCAT-Tailing Boosts GBM Cell Migration and Resistance to Apoptosis

The elevated mitochondrial membrane potential (ΔΨm) and constricted MPTP resulting from msiCAT-tailed ATP5□ and other mitochondrial proteins may enhance cellular stress resilience. We first investigated how the msiCAT-tailing mechanism affects GBM cells at the cellular level. MTT assays (52) revealed that overexpressing short (AT3) and long (AT20) AT repeat tails, fused to ATP5□, significantly improved GBM cell viability, but not that of NHA cells (Fig. 4A, B). However, short (GS3) and long (GS20) GS repeat tails did not affect GBM cell viability (Fig. S7A). In addition, *in vitro* transwell migration assays (53) and wound healing assays (54) showed that GBM cells overexpressing AT repeat-tailed ATP5α exhibited increased cell invasion and accelerated wound healing, indicating enhanced cell migration (Fig. 4C, D, S7B, C). Notably,

neither ATP5α alone nor GS repeat-tailed proteins showed comparable changes (Fig. S7D, E). Furthermore, overexpressing AT3- and AT20-tailed proteins effectively conferred phenotypes associated with increased GBM cell activity, such as enhanced survival and migration, even with inhibited endogenous CAT-tailing machinery activity (e.g., sgNEMF and oeANKZF1) (Fig. 4E-G). It is worth noting that ANKZF1 knockdown in U87 and U251 cell lines can cause aberrant mitoGFP accumulation, possibly reducing cellular adaptability (29), suggesting varying mitochondrial adaptability to proteostasis stress across cell lines. Supporting this, initial experiments showed that mild expression of ATP5α-AT3 and ATP5α-AT20 did not induce strong mitochondrial proteotoxic responses, as evidenced by the lack of significant upregulation in *LONP1*, *mtHSP70*, and *HSP60* mRNA levels (Fig. S7F).

GBM cells exhibit increased resistance to staurosporine (STS)-induced apoptosis, supported by fewer TUNEL-positive cells (Fig. S8A, B) and markedly diminished PARP-1 (Poly ADP-ribose polymerase) cleavage (Fig. S8C), a marker of AIF-mediated apoptosis (55). To investigate the role of CAT-tailed ATP5α proteins in this resistance, we overexpressed proteins with mimetic tails in GBM cells. Overexpression of both short tail (ATP5α-AT3) and long tail (ATP5α-AT20) significantly enhanced resistance to STS-induced apoptosis, as shown by TUNEL staining (Fig. 4H, I) and flow cytometry (Fig. S8D, E), indicating a strong link between protein CAT-tailing and tumorigenesis. In contrast, control short (GS3) and long (GS20) GS tails failed to confer such resistance (Fig. S8F, G). Consistent with these findings, overexpression of artificial CAT-tailed ATP5α proteins also increased the resistance of GBM cells to temozolomide (TMZ)-induced apoptosis (Fig. 4J). Taken together, these results suggest that RQC-induced CAT-tailing on ATP5α protein plays a role in GBM resistance to drug-induced apoptosis.

GBM Cell Progression is Hindered by RQC Pathway Inhibition

Prior research indicates the RQC pathway's mediated msiCAT-tailing plays an important role in GBM progression, suggesting it as a potential therapeutic target. To explore this, patient-derived Glioblastoma Stem Cell (GSC) lines were treated with anisomycin, an inhibitor of CAT-tailing. GSC lines displayed higher sensitivity to anisomycin than normal neural stem cells (NSCs) (Fig. 5A). Similarly, genetic inhibition of the RQC pathway via NEMF knockdown (sgNEMF) or ANKZF1 overexpression (oeANZKF1) in the SF268 GBM cell line also suppressed GBM growth (Fig. 5B). Notably, control NHA cell proliferation was also inhibited by these genetic changes, indicating the broad significance of NEMF and ANKZF1 in cell proliferation (Fig. 5C). The RQC pathway appears to have a more pronounced effect on GBM cell migration. In *in vitro* transwell assays, sgNEMF or oeANZKF1 notably decreased GBM cell migration without affecting NHA cells (Fig. 5D, E). Consistently, anisomycin treatment impaired GSC cell migration, but not NHA cell migration (Fig. 5F, G).

Further investigation revealed the RQC pathway's involvement in GBM cell anti-apoptosis, with initial findings pointing to alterations in mitochondrial functions. Prior studies demonstrated that genetic or pharmacological inhibition of the RQC pathway led to a significant decrease in GBM mitochondrial membrane potential ($\Delta\Psi m$) (Fig. 2C, D). In GSC cells, anisomycin treatment promoted mitochondrial permeability transition pore (MPTP) opening, an effect not seen in NHA cells (Fig. 3A-D). Consequently, GBM cell lines with genetically or pharmacologically inhibited RQC pathways were more susceptible to STS-induced apoptosis, evidenced by elevated executioner caspase 3/7 activity (Fig. S9A), enhanced PARP-1 cleavage (Fig. S9B, C), increased TUNEL staining (Fig. 5H-K), and flow cytometry analysis (Fig. S9D-G). Notably, general translation inhibition using cycloheximide did not elicit the same apoptotic

response (Fig. S9A, D, E). Finally, the RQC pathway was also implicated in temozolomide (TMZ)-induced cell death. Combining anisomycin with TMZ significantly reduced GBM cell survival (Fig. 5L) and effectively inhibited GSC spheroid growth (Fig. 5M, N). In summary, the RQC pathway plays a critical role in multiple aspects of GBM progression, including proliferation, migration, and survival under apoptotic stress.

Discussion

The Ribosome-associated Quality Control (RQC) pathway plays a crucial role in managing aberrant proteins produced during translation. This study focused on understanding the consequences of RQC-mediated modification, specifically the addition of msiCAT tails, to mitochondrial proteins like ATP5α in glioblastoma (GBM) cells. The findings reveal that GBM cells harboring msiCAT-modified ATP5α exhibit a unique metabolic profile. Despite a reduction in ATP synthesis, these cells maintain their mitochondrial membrane potential ($\Delta\Psi m$), a key factor for cellular function and survival. Furthermore, they demonstrate enhanced cell survival and motility, characteristics associated with increased tumor invasiveness and metastasis. Notably, the presence of msiCAT-modified ATP5α confers resistance to apoptosis triggered by staurosporine (STS), potentially by modulating the mitochondrial permeability transition pore (MPTP), a critical regulator of cell death pathways, as illustrated in Figure 6. These identified traits contribute to an increased aggressiveness of tumors, suggesting that the RQC pathway plays a critical role in cancer cell survival and proliferation. Encouragingly, a recent study also demonstrated the RQC pathway's involvement in a *Drosophila* Notch overexpression-induced brain tumor model (56). The findings imply modulating the RQC pathway could serve as a promising complementary strategy to existing chemotherapy regimens. By targeting this specific pathway, therapeutic interventions might effectively disrupt the mechanisms that allow cancer cells to evade apoptosis and sustain their energy production under stress, potentially leading to improved treatment outcomes for patients with GBM and other cancers characterized by similar protein modifications.

The study of ATP synthase behavior in cancer holds particular importance. During carcinogenesis, ATP synthase frequently relocates to the plasma membrane, where it is termed

ectopic ATP synthase (eATP synthase). These eATP synthases exhibit catalytic activity, facilitating ATP production in the extracellular space to foster a favorable tumor microenvironment (57). Research indicates that eATP synthase assembles initially in mitochondria before being transported to the cell surface via microtubules (47). However, the specific type of ATP synthase delivered to the plasma membrane remains unclear. Future investigations into the localization of CAT-tailed eATP synthase may offer valuable insights into this process.

Multiple mitochondrial proteins in cancer cells can likely undergo CAT-tailing in a similar way. These msiCAT-tailed peptides may have varied impacts on mitochondria and cells due to differences in their base proteins. For instance, CAT-tailed COX4 protein might substantially and directly diminish mitochondrial respiratory efficiency. Examining the individual roles of these proteins is important, as the combined effect of their defects may be crucial in understanding observed mitochondrial changes in cancer. A minor caveat here is that the observed effect of the CAT-tails' presence primarily stems from artificial CAT-tail sequences with a high threonine content, rather than the endogenous CAT-tail protein. It is possible that other sequence components could lead to different effects (44). A recent study found that ANKZF1 knockdown inhibited GBM progression by causing abnormal protein accumulation in mitochondria (29). This, combined with our data, suggests that balanced ANKZF1 expression and activity are vital for cancer proliferation. Both excess and deficiency may alter cellular adaptability. A minor flaw of that study was the use of a mitochondrial-localized non-stopped GFP protein to induce proteostasis stress and the lack of direct biochemical evidence of CAT-tailed proteins. Our research focuses on endogenous proteins for a detailed analysis of their impact on mitochondria. The rationale is that highly expressed, non-physiological ectopic

proteins might cause general proteostasis failure, masking the specific functions of endogenous proteins. Additionally, the studies used different cell lines. GSC, a patient-derived GBM cell line with greater stemness, might have distinct mitochondrial status and RQC pathway activity compared to U87 or U251 cell lines. Thus, the conclusions of the two studies are not contradictory but rather complementary, both demonstrating the significance of RQC in tumorigenesis. Our study delves into the mechanistic role of the RQC pathway in GBM, identifying new potential targets for future treatments.

An in-depth investigation into the quantification of nuclear genome-encoded mitochondrial proteins modified via the msiCAT-tailing mechanism using sophisticated mass spectrometry is a compelling area for future research. Recent work by Lv et al., published in *Cell Reports*, revealed that the cytoplasmic E3 ligase Pirh2 and the mitochondrial protease ClpXP work in conjunction with the established NEMF-ANKZF1 system to break down mitochondrial protein aggregates resulting from ribosome stalling (58). The increased presence of ClpXP in various cancers could potentially be linked to an increase in msiCAT-tailing products in mitochondria, though further studies are needed to clarify ClpXP's role in mitochondrial RQC (59). Moreover, ClpXP influences the levels of multiple mitochondrial proteins. Our own experiments showed that ATP5α proteins lacking msiCAT-tails were the most challenging to express ectopically. Proteins with shorter tails (AT3) expressed more readily, while those with longer tails (AT20) exhibited the highest expression levels but also tended to form SDS-insoluble aggregates. This regulatory effect could be mediated by ClpXP-dependent degradation or potentially through transcriptional control. PGC-1α, the peroxisome proliferator-activated receptor gamma co-activator, is a key regulator of mitochondrial biogenesis in mammals (60). By binding to and activating nuclear transcription factors, PGC-1α triggers the transcription of

nuclear genome-encoded mitochondrial proteins and the mitochondrial transcription factor Tfam. Tfam, in turn, activates mitochondrial genome transcription and replication (61). Distinguishing between these regulatory possibilities will necessitate future research, including a meticulous examination of mRNA levels for msiCAT-tailed targets and analysis of PGC-1α and Tfam binding to transcriptional elements.

MPTP is a complex, supramolecular channel traversing the inner mitochondrial membrane, characterized by its non-selective ion permeability, calcium dependence, and multifaceted functionality. Despite extensive investigations into its functional attributes and regulatory mechanisms, the precise molecular architecture of the MPTP remains elusive (62). Several theoretical models have been posited to elucidate the MPTP's structural composition. Firstly, the VDAC/ANT/Cyp-D model (63) proposed an assembly of voltage-dependent anion channels (VDAC), adenine nucleotide translocators (ANT), and cyclophilin D (Cyp-D) as the structural basis; however, subsequent genetic analyses have introduced substantial controversy regarding the integral role of these proteins within the MPTP complex (64-67). Secondly, the ATP synthase model posits that MPTP formation involves dimers or reconstituted c-rings of ATP synthase (48, 49). While this hypothesis presents an intriguing perspective, empirical confirmation of ATP synthase’s role as a definitive structural element of the pore remains inconclusive, with a body of conflicting research surrounding this proposition. Thirdly, the contemporary prevailing hypothesis suggests the MPTP is constituted by a large complex, termed the ATP synthasome, comprising ANT and ATP synthase, with Cyp-D serving a regulatory function over the complex’s dynamic behavior (68).

The MPTP activity is modulated by mitochondrial membrane potential ($\Delta\Psi m$), which reciprocally influences mitochondrial ion homeostasis and energy metabolism (69, 70). Our

study elucidates a dual function of msiCAT-tailed ATP5α protein in cancer cells: stabilization of a high membrane potential, thereby mitigating MPTP induction, and direct inhibition of MPTP functionality through participation in its assembly. While MPTP's critical role in cell death is established, the premise that MPTP inhibition enables cancer cell evasion of drug-induced programmed cell death has lacked substantial evidence. This study furnishes empirical support for this hypothesis, demonstrating that GBM cells, notably glioblastoma stem cells (GSC), exhibit markedly reduced MPTP activity relative to control cells. This reduced activity is directly correlated with the CAT-tailing modification of the ATP synthase subunit. These observations are concordant with prior research indicating that genetic mutations or post-translational modifications in specific ATP synthase subunits can modulate MPTP activity. The findings highlight a novel mechanism through which cancer cells may develop resistance to therapeutic interventions by manipulating mitochondrial function (71, 72).

Materials and Methods

Cell lines and cell culture conditions

The human astroglia cell line SVG p12 (ATCC, cat. CRL-8621) and the human glioma cell line SF268 were from Dr. Rongze Olivia Lu. Both cell lines were cultured in DMEM (ATCC, cat. #302002) with 10% FBS (Biowest, cat. S1620-100) and penicillin/streptomycin (Gibco™, cat. 15140122). SF268 clones should be maintained in complete DMEM supplemented with 400 µg/mL G418 (Gibco, cat. 10131027). The 0.25% trypsin solution (ATCC, cat. #SM2003C) was used to passage cells. The normal human astrocytes NHA E6/E7/hTERT cell line was from Dr. Russell O. Pieper, UCSF Brain Tumor Research Center. Cells are cultured in ABM™ Basal Medium (Lonza, cat. CC-3187) and AGM™ SingleQuots™ Supplements (Lonza, cat. CC-4123). Corning™ Accutase™ Cell Detachment Solution (Corning, cat. 25058CI) was used to passage cells. GSC827, a patient-derived human glioma stem cell line, was from Dr. Chun-Zhang Yang at NIH. The NSC, NSC26, patient-derived GSC33, GSC22, GSC99, GSC105, and GSC107 cell lines used in this study were kindly provided by Dr. John S Kuo at the University of Texas, Austin. GSC cells were cultured in Neural basal-A Medium (Gibco, cat. #10888022) with 2% B27 (Gibco, cat. #17504044), 1% N2 (Gibco, cat. #17502048), 20 ng/ml of EGF and FGF (Shenandoah Biotechnology Inc. cat. PB-500-017), Antibiotic-Antimycotic (Gibco, cat. #15240062), and L-Glutamine (Gibco, cat. #250300810). Cells could be cultured in both spherical and attached (on Geltrex, Thermo Fisher, cat. A1413202) forms. Corning™ Accutase™ Cell Detachment Solution (Corning, cat. 25058CI) was used to passage cells.

Cells were transfected with X-tremeGENE™ HP DNA Transfection Reagent (Sigma, cat. 6366244001) following the standard protocol. For single clone selection, SF268 cells were treated with 800 µg/ml G418 for 5 days. The cells were then seeded into a 96-well plate at a

density of 1/100 μL. Positive clones were verified by immunofluorescence staining and immunoblotting. Cells were maintained in complete DMEM containing 400 μg/mL G418. GBM cell lines were subjected to a 4-hour pre-treatment at 37°C using either anisomycin (20 nM or 200 nM, Fisher Scientific, cat. AAJ62964MF) or cycloheximide (100 μg/mL, Fisher Scientific, cat. AC357420010) in medium, as detailed in the conducted experiments.

Primers, plasmids and viruses

Plasmids pcDNA3.1+/C-(K)-DYK-ATP5F1A (pATP5 control), pcDNA3.1+/C-(K)-DYK-ATP5F1A-AT3 (pATP5-AT3), pcDNA3.1+/C-(K)-DYK-ATP5F1A-AT20 (pATP5-AT20), pcDNA3.1+/C-(K)-DYK-ATP5F1A-GS3 (pATP5-GS3), and pcDNA3.1+/C-(K)-ATP5F1A-DYK-GS20 (pATP5-GS20) were generated by GenScript Inc. Plasmids pCMV-5×FLAG-β-globin-control (5FBG-Ctrl) and pCMV-5×FLAG-β-globin-non-stop (5FBG-nonstop) were generated by Dr. Hoshino (Nagoya City University) and Dr. Inada (Tohoku University) (43). pCMV6-DDK-NEMF (oeNEMF) was from ORIGENE Inc. (cat. RC216806).

Viruses (and plasmid used to generate viruses) are pLV[CRISPR]-hCas9:T2A:Neo-U6>Scramble[gRNA#1] (sgControl/sgCtrl), pLV[CRISPR]-hCas9:T2A:Neo-U6>hNEMF[gRNA#1579] (sgNEMF), pLV[Exp]-Bsd-EF1A>ORF_Stuffer (pLV-control), pLV[Exp]-EGFP:T2A:Puro-EF1A>mCherry (pLV-control-2/oeCtrl), pLV[Exp]-Bsd-EF1A>hANKZF1[NM_001042410.2]/HA (oeANKZF1), and pLV[Exp]-mCherry/Neo-EF1A>hANKZF1[NM_001042410.2] (oeANKZF1) were made by VectorBuilder Inc.

Primers (5’ to 3’) used for RT-PCR are:

LONP1	lonp1_forward: TGCCTTGAACCCTCTCTAC
	lonp1_reverse: TCTGCTTGATCTTCTCCTCC
mtHSP70	mthsp70_forward: ACTCCTCCATTTATCCGCC
	mthsp70_reverse: ACCTTTGCTTGTTTACCTTCC
HSP60	hsp60_forward: ACCTGCTCTTGAAATTGCC
	hsp60_reverse: CAATCCCTCTTCTCCAAACAC
ACTB	actb_forward: TGTTTGAGACCTTCAACACC
	actb_reverse: ATGTCACGCACGATTTCC

Neurosphere formation assay of GSCs

The GSC spheroids were dissociated using Accutase for 2 min. Cells were resuspended in a single-cell suspension and grown under non-adherent conditions. Cells were seeded in 12-well plates at a density of 0.25×10^6 cells/well and cultured in 3 mL culture medium for 24 hours. 20 nM of anisomycin and 150 µM of temozolomide (TMZ) were added to the culture medium and treated for 96 hours. Spheroids were imaged under a 10x objective, captured using QCapture, and analyzed with ImageJ. Spheroids larger than 50 µm were counted.

Differential gene expression analysis using the public database

The raw RNA-seq data used to perform the analysis were obtained from the University of California, Santa Cruz Xenabrowser (cohort: TCGA TARGET GTEx, dataset ID: TcgaTargetGtex_rsem_gene_tpm, https://xena.ucsc.edu/), and then subsets included only TCGA glioma (GBM), GTEx Brain Frontal Cortex, and GTEx Cortex samples. Differential expression

analysis was conducted using the “Limma” package (R version: 4.3.1). The Benjamini-Hochberg method was used for multiple testing correction to control the false discovery rate (FDR). Cut-off of adjusted p-value (adj.P.Val) was set at 0.001; cut-off of the absolute fold change was set at 2 (logFC > 1).

Immunostaining

Cells were cultured on sterile coverslips until 80% confluency. For immunostaining, cells were washed with phosphate-buffered saline (PBS) solution thrice. Then, 4% formaldehyde (Thermo Fisher, cat. BP531-500) was applied to cells for fixation for 30 min at room temperature. After fixation, cells were washed with PBS solution containing 0.25% Triton X-100 (PBSTx) (Thermo Fisher, cat. T9284) thrice, and blocked with 5% normal goat serum (Jackson Immuno, cat. 005-000-121) for 1 hour at room temperature. Cells were then incubated with primary antibodies overnight in a humidified chamber at 4°C. The next day, cells were washed by PBSTx thrice and incubated with secondary antibodies for 2 hours at room temperature. After washing, cells were stained with 300 nM DAPI (Thermo Fisher, cat. 57-481-0) for 5 min at room temperature and mounted in Fluoromount-G Anti-Fade solution (Southern Biotech, cat. 0100-35). Images were taken using a Zeiss LSM 800 confocal microscope, 40x oil objective lens, and AiryScan processing. The primary antibodies used in the study were rabbit anti-ATP5a (Cell Signaling, cat. #18023), mouse anti-TOMM20 (1:500, Santa Cruz, cat. 18023S), rabbit anti-MTCO2 (1:500, Abclonal, cat. sc-17764), and mouse anti-NDUS3 (1:1000, Abcam, cat. ab14711). The secondary antibodies were Alexa fluor 633-, 594-, 488-conjugated secondary antibodies (1:300, Invitrogen, cat. A21071, A11036, A32732).

SDS-PAGE and immunoblotting

Cells or isolated mitochondria were solubilized in cell lysis buffer containing 50 mM Tris-HCl pH 7.4, 150 mM NaCl, 10% glycerol, 1% Triton X-100, 5 mM EDTA, and 1x protease inhibitor (Bimake, cat. B14002). Protein concentration was measured by using the Bradford assay (BioVision, cat. K813-5000-1). Samples were separated in a 4-12% Tris-Glycine gel (Invitrogen, cat. WXP41220BOX) and proteins were transferred to a PVDF membrane (Millipore, cat. ISEQ00010). The membranes were then blocked with 5% non-fat dry milk (Kroger) for 50 min at room temperature and probed with primary antibodies overnight at 4°C. Membranes were washed with Tris-buffered saline with 0.1% Tween 20 (TBST) solution thrice and then incubated with secondary antibodies for 1 hour at room temperature. Blots were detected with ECL solution (PerkinElmer, cat. NEL122001EA) and imaged by Chemidoc system (BioRad). The intensity of blots was further analyzed by ImageJ software. The primary antibodies used were mouse anti-Actin (1:1000, Santa Cruz, cat. sc-47778), rabbit anti-NEMF (1:1000, Proteintech, cat. 11840-1-AP), mouse anti-ANKZF1 (1:1000, Santa Cruz, cat. sc-398713), mouse anti-ATP5a (Abcam, cat. ab14748), mouse anti-NDUS3 (1:1000, Abcam, cat. ab14711), rabbit anti-COX4 (Abcam, cat. ab209727), mouse anti-Flag (1:1000, Sigma, cat. F1804), rabbit anti-ANT1/2 (1:1000, Proteintech, cat. 17796-1-AP), rabbit anti-CypD (1:1000, Proteinetch, cat. 15997-1-AP), rabbit anti-PARP1 (1:1000, Abclonal, cat. A0942), rabbit anti-GAPDH (1:1000, Abclonal, cat. A19056). The secondary antibodies used were goat anti-rabbit IgG (1:5000, Invitrogen, cat. G21234), goat anti-mouse IgG (1:5000, Invitrogen, cat. PI31430).

Mitochondrial isolation, blue Native PAGE, and western blotting

Cells were homogenized using Dounce homogenizer in ice-cold homogenization buffer

containing 210 mM mannitol (Fisher Sci, cat. AA3334236), 70 mM sucrose (Fisher Sci, cat. AA36508A1), 5 mM HEPES (Fisher Sci, cat. 15630106), pH 7.12, 1 mM EGTA (Fisher Sci, cat. 28-071-G), and 1x protease inhibitor. The homogenate was centrifuged at 1500 g for 5 min. The resultant supernatant was centrifuged at 13000 g for 17 min. The supernatant was collected as the cytosol portion, and the pellet as the mitochondria portion, was washed with homogenization buffer and centrifuged at 13000 g for 10 min. For Blue Native PAGE, the mitochondria samples were solubilized in 5 % digitonin (Thermo Fisher, cat. BN2006) on ice for 30 min and then centrifuged at 20000 g for 30 min. The supernatant contains solubilized mitochondrial proteins and was mixed with 5% G-250 (GoldBio, cat. C-460-5) and 1x NativePAGE sample buffer (Invitrogen, cat. BN2008) (final G-250 concentration is 25% of the digitonin concentration). Mitochondrial protein concentration was measured by using the Bradford assay. Samples were separated in 3-12% Bis-Tris Native gel (Invitrogen, cat. BN1001BOX) and then transferred to a PVDF membrane. Membranes were fixed with 8% acetic acid (Thermo Fisher, cat. 9526-33), and then blocked and probed with antibodies as described above for Western blotting.

Mitochondrial membrane potential assays

Mitochondrial membrane potential of GSC cells was measured using Image-iT™ TMRM (Invitrogen, cat. I34361). Cells were cultured in the 96-well black plate at a density of 1 x10^5 cells per well overnight in an incubator with 5% CO_2 at 37°C. Cells were incubated with TMRM (100 nM) for 30 min at 37°C. Then, cells were washed with PBS solution three times. Fluorescence changes at excitation/emission of 548/574 nm were monitored with a Cytation 5 plate reader (BioTek). Mitochondrial membrane potential was also measured using JC-10 (AdipoGen, cat. 50-114-6552). Cells were cultured in the 96-well black plate at a density of 5 x

10^4 cells per well overnight in an incubator with 5% CO_2 at 37°C. Cells were incubated with JC-10 (10 μg/ml) for 45 min at 37°C. Then, cells were washed with PBS solution twice. Fluorescence changes at excitation/emission of 535/595 nm for JC-10 aggregates and at 485/535 nm for JC-10 monomers were monitored with a Synergy 2 Reader (BioTek). Mitochondrial membrane potential was quantified as the fluorescence of JC-10 aggregates/monomers (595/535 nm).

Seahorse cell mitochondrial stress assays

The oxygen consumption rate (OCR) of cells was measured using the Seahorse Cell Mito Stress Test kit following the user guide (Agilent, cat. 103010-100). Briefly, cells were cultured in testing chambers at a density of 8000 cells per well overnight in an incubator with 5% CO_2 at 37°C. Cells were then washed with assay medium containing Seahorse XF DMEM medium (Agilent, cat. 103575-100) with 1 mM pyruvate, 2 mM glutamine, and 10 mM glucose twice, and incubated in assay medium for 1 hour in an incubator without CO_2 at 37°C. Cells were treated with compounds in the order of oligomycin (1.5 μM), carbonyl cyanide-4 (trifluoromethoxy), phenylhydrazone (FCCP, 1.0 μM), and Rotenone/Antimycin (0.5 μM). The OCR of cells was monitored by using Seahorse XF HS Mini (Agilent).

Mitochondrial MPTP assay

The status of mitochondrial permeability transition pore was measured using Invitrogen™ Image-IT™ LIVE Mitochondrial Transition Pore Assay Kit (Invitrogen, cat. I35103). Cells were cultured in 35 mm glass-bottom dishes overnight in an incubator with 5% CO_2 at 37°C. Cells

were washed twice with the modified Hank's Balanced Salt Solution (HBSS, Thermo Fisher, cat. 14025092) containing 10 mM HEPES, 2 mM L-glutamine and 0.1 mM succinate (Thermo Fisher, cat. 041983.A7) and incubated with the labeling solution (1 μM Calcein, 0.2 μM MitoTracker Red, 1 mM Cobalt Chloride) for 15 min at 37°C. Cells were then washed with HBSS twice and imaged at excitation/emission of 494/517 nm for Calcein and at 579/599 nm for MitoTracker Red by using the Zeiss confocal microscope.

Mitochondrial Ca^{2+} retention capacity assay

The mitochondrial calcium retention capacity (CRC) was measured on a Cytation 5 reader at excitation/emission of 506/592 nm using the membrane-impermeable fluorescent probe Calcium green-5N (Invitrogen, cat. C3737). Isolated mitochondria samples (0.75 mg protein/mL) were incubated in 1 mL swelling medium supplemented with 10 mM succinate, 1 μM Calcium green-5N, inorganic phosphate, and cyclosporine A (Thermo Fisher, cat. AC457970010). One Ca^{2+} addition was 1.25 nmol (1 mL volume). Only the MPTP opening in the presence of cyclosporine A was induced by high amounts of added calcium (30 nmol Ca^{2+} in the last two additions). The CRC value was calculated as total Ca^{2+} accumulated in the mitochondria per unit (1 mg protein).

MTT assay

Cell proliferation was measured by using the MTT assay kit (Roche, cat. 11465007001). Cells were cultured in 96-well plates at a density of 2000 cells per well overnight in an incubator with 5% CO_2 at 37°C. Cells were treated with MTT labeling reagent for 4 hours at 37°C. The solubilization buffer was added to the cells, and then the cells were incubated overnight at 37°C.

Absorbance changes of the samples at 550 nm were monitored by using a Synergy 2 Reader (BioTek).

Wound healing assay

Cells were seeded into 6-well plates and cultured for 24-48 hours to reach a confluent cell monolayer. Cells were treated with serum-free medium overnight before mechanical scratching (54). Images of the wounds were taken at 0, 24, and 48 hours. Wound areas were measured by using the wound healing plugin of ImageJ. Wound Coverage % = 100% x $[A_{t=0h}-A_{t=\Delta h}]/A_{t=0h}$ ($A_{t=0h}$ is the area of the wound measured immediately after scratching $t = 0h$, $A_{t=\Delta h}$ is the area of the wound measured h hours after the scratch is performed).

Cell migration assay

Cell migration was measured by using Transwell assays (Corning, cat. CLS3422). Cells were cultured in Transwell inserts at a density of 1 x 10^5 cells per well for 3 hours in an incubator at 37°C with 5% CO_2. The top inserts were supplemented with DMEM medium only, and the bottom wells were supplemented with DMEM medium with 20% Fetal Bovine Serum. After incubation, the cells on the apical side of the Transwell insert membrane were removed using a cotton applicator. The cells on the bottom side of the insert were rinsed with PBS twice and fixed in 70% ethanol (Thermo Fisher, cat. R40135) for 15 min at room temperature. After fixation, inserts were placed into an empty well to allow the membrane to dry. Then, the insert was incubated with 0.2% crystal violet (Sigma, cat. V5265) for 5 min at room temperature. The insert was rinsed with water twice, and images were captured by using a microscope with a 20x

objective. Cell numbers were quantified using ImageJ.

TUNEL staining

The apoptosis was measured by a TUNEL assay kit (ApexBio, cat. K1134). Cells were cultured on sterile cover slips until 80% confluency and washed with PBS thrice. Then, 4% formaldehyde was applied to cells and fixed for at 4°C 25 min. After fixation, cells were washed with PBS twice and incubated with 20 μM proteinase K (Invitrogen, cat. 25530049) for 5 min at room temperature. Then, cells were rinsed with PBS thrice and incubated in 1x equilibration buffer for 10 min at room temperature. Cells were stained with FITC or Cy3 labeling mix for 1 hour at 37°C in a humidified chamber. Cells were washed by PBS thrice and stained with DAPI for 5 min at room temperature. Cells were mounted in the Fluoromount-G Anti-Fade solution and imaged at 520 nm for FITC or at 570 nm for Cy3 by using the Zeiss confocal microscope.

Caspase-3/7 activity assay

Caspase-3/7 activity was measured by using CellEvent™ Caspase□3/7 Detection Reagents (Invitrogen, cat. C10432) following the manufacturer's protocol. Specifically, cells were seeded in a 96-well black plate with a clear bottom at a density of 5 x 10^4 cells per well and incubated overnight in the incubator with 5% CO_2 at 37°C. Cells were then incubated with 1x staining solution for 30 min at 37°C. Fluorescence changes at excitation/emission of 485/525 nm were monitored with a Synergy 2 Reader (BioTek).

Annexin V-FITC/Propidium Iodide (PI) apoptosis detection

Annexin V-FITC/PI apoptosis assay was performed by using the FITC Annexin V Apoptosis Detection Kit with PI (BioLegend, cat. 640914). Briefly, 1 x 10^5 cells were collected in 100 μL of staining buffer. Then, cells were incubated with 5 μL of Annexin V-FITC and 2.5 μL of PI for 15 min at room temperature in the dark. Following incubation, 400 μL of binding buffer was added to the stained cells. Flow cytometry analysis of the fluorescence was performed using a Soni SH800 Cell Sorter.

Mitochondria ATP measurement via fluorescence imaging of ATP-red

BioTracker™ ATP□red dye (Millipore, cat. SCT045) is a fluorogenic indicator for ATP in mitochondria (73). Cells cultured in monolayer conditions were incubated in medium with 5□μM ATP□red for 15□min in an incubator at 37°C with 5% CO_2. Mitochondria were also labeled by incubating cells with 100 nM MitoTracker-Green (Invitrogen, cat. M7514) for 15 min to normalize their mass. Before measurement, cells were washed twice with culture medium, and then fresh medium was added. Cells were imaged in a 37°C chamber with 5% CO_2 at excitation/emission of 510/570 nm for ATP-red and at excitation/emission of 490/516 nm for MitoTracker-Green by using the Zeiss confocal microscope. The ATP-red signals could also be measured by a Synergy 2 Reader (BioTek).

Co-immunoprecipitation

Cells were lysed in the buffer containing 50 mM Tris-HCl pH 7.4, 150 mM NaCl, 10% glycerol,

1% TritonX-100, 5 mM EDTA, and 1x protease inhibitor. Soluble samples were incubated with 1.5 μL ATP5 antibody at 4°C with mixing overnight. 25 μL of protein A/G magnetic beads (Pierce, cat. 88802) were added to the co-IP samples and incubated at 4°C with mixing overnight. Samples were washed with washing buffer thrice and then applied to SDS-PAGE analysis.

Mice and immunostaining

Animal studies were approved by the University of California, San Francisco Institutional Animal Care and Use Committee (IACUC, AN195636-01) and were performed following the guidelines of the National Institutes of Health (NIH).

For orthotopic brain tumor models, 8-to-10-week-old C57BL/6 mice (male and female in equal numbers) were used for i.c. studies. Cell lines (GL261, SB28) were suspended in DMEM for inoculation. Mice were anesthetized with isoflurane, and 30,000 tumor cells were injected orthotopically in 3 μL. Using a stereotactic frame, a burr hole was formed on the skull via a 0.7 mm drill bit 1.5mm laterally to the right and 1.5mm rostrally from the bregma, and a noncoring needle (26s gauge; Hamilton) was used to inject the cells at a depth of 3mm into the brain from the burr hole. The skin incision was sutured. Mice were then monitored daily. Mouse SB28 tumor tissue and wild-type mouse brain tissue were collected at the survival endpoint.

Frozen tissue sections were thawed at room temperature for 20 min and rinsed with PBS three times. Tissues were then fixed in 4% formaldehyde for 15 min at room temperature. After washing in PBS, tissues were permeabilized with 0.01% Triton X-100 + 0.1% Tween-20 for 15 min and then blocked by using 5% normal goat serum and M.O.M. blocking reagent (Vector

Laboratories, cat. BMK-2202) for 1 hour at room temperature. Tissues were then incubated with primary antibodies overnight in a humidified chamber at 4°C. After washing in PBST, tissues were incubated with secondary antibodies for 1 hour. After washing again in PBST, tissues were stained with 300 nM DAPI for 5 min and mounted in Fluoromount-G Anti-Fade solution. Images were taken using a Zeiss LSM 800 confocal microscope. The primary antibodies used in the study were mouse anti-ATP5a (1:500, Abcam, cat. Ab14748), rat anti-TOMM20 (1:500, Abcam, cat. Ab289670), rabbit anti-NEMF (1:500, Proteintech, cat. 11840-1-AP), mouse anti-ANKZF1 (1:500, Santa Cruz, cat. sc-398713), chicken anti-GFP (1:500, Abcam, cat. Ab13970). The secondary antibodies were Alexa Fluor 633-, 594-, 488-conjugated secondary antibodies (1: 300, Invitrogen, cat. A21071, A11036, A32732).

Statistics

Statistical analyses were performed by using GraphPad 7.0 software. Chi-squared test and unpaired Student's t-test were used for comparison. $P < 0.05$ was considered significant, except in gene expression analysis (Fig. 1A). *, $P < 0.05$; **, $P < 0.01$; ***, $P < 0.001$; ****, $P < 0.0001$; ns, not significant. All data were expressed as means ± s.e.m.

Acknowledgements

We are grateful to Dr. Chunzhang Yang at the National Cancer Institute and Dr. Russell O. Pieper at the University of California, San Francisco, for the cell lines. We thank Dr. Hoshino at Nagoya City University and Dr. Inada at Tohoku University for providing the plasmids. We also thank members of the Wu lab at Southern Methodist University and members of the Lu lab at UCSF for their help and discussions. This work was supported by the NIH (R35GM150190 to ZW), the Southern Methodist University Dedman College Dean's Research Council grant (to ZW), the Cancer Prevention and Research Institute of Texas (RP210068 to ZW and RL), and the SPARK-South Carolina Alzheimer's Disease Research Center (ARDC) Pilot Grant (to QL).

Author contributions

BZ and TC designed, performed the experiments, analyzed the data, and wrote the manuscript. BZ, TC, ER, YW, AG, YT, IM, JW, YS, QL, and WH performed the experiments and analyzed the data. RL and ZW formed the idea, supervised the project, wrote the manuscript, and provided funding.

Conflict of interest

The authors declare no competing interests.

Materials availability

Plasmids and other materials generated in this study will be available upon request from the lead

contact with a completed Materials Transfer Agreement.

References

1. Robichaud N, et al. Translational Control in Cancer. *Cold Spring Harbor perspectives in biology.* 2019;11(7).
2. Dever TE, and Green R. The elongation, termination, and recycling phases of translation in eukaryotes. *Cold Spring Harbor perspectives in biology.* 2012;4(7).
3. Kim KQ, and Zaher HS. Canary in a coal mine: collided ribosomes as sensors of cellular conditions. *Trends in biochemical sciences.* 2022;47(1).
4. Brandman O, et al. A ribosome-bound quality control complex triggers degradation of nascent peptides and signals translation stress. *Cell.* 2012;151(5).
5. Juszkiewicz S, and Hegde RS. Initiation of Quality Control during Poly(A) Translation Requires Site-Specific Ribosome Ubiquitination. *Molecular cell.* 2017;65(4).
6. Sundaramoorthy E, et al. ZNF598 and RACK1 Regulate Mammalian Ribosome-Associated Quality Control Function by Mediating Regulatory 40S Ribosomal Ubiquitylation. *Molecular cell.* 2017;65(4).
7. Hashimoto S, et al. Identification of a novel trigger complex that facilitates ribosome-associated quality control in mammalian cells. *Scientific reports.* 2020;10(1).
8. Juszkiewicz S, et al. The ASC-1 Complex Disassembles Collided Ribosomes. *Molecular cell.* 2020;79(4).
9. Shao S, and Hegde RS. Reconstitution of a minimal ribosome-associated ubiquitination pathway with purified factors. *Molecular cell.* 2014;55(6).
10. Shen PS, et al. Protein synthesis. Rqc2p and 60S ribosomal subunits mediate mRNA-independent elongation of nascent chains. *Science (New York, NY).* 2015;347(6217).
11. Verma R, et al. Vms1 and ANKZF1 peptidyl-tRNA hydrolases release nascent chains

from stalled ribosomes. *Nature.* 2018;557(7705).

12. Kostova KK, et al. CAT-tailing as a fail-safe mechanism for efficient degradation of stalled nascent polypeptides. *Science (New York, NY).* 2017;357(6349).

13. Lytvynenko I, et al. Alanine Tails Signal Proteolysis in Bacterial Ribosome-Associated Quality Control. *Cell.* 2019;178(1).

14. Sitron CS, et al. Aggregation of CAT tails blocks their degradation and causes proteotoxicity in S. cerevisiae. *PloS one.* 2020;15(1).

15. Choe YJ, et al. Failure of RQC machinery causes protein aggregation and proteotoxic stress. *Nature.* 2016;531(7593).

16. Yonashiro R, et al. The Rqc2/Tae2 subunit of the ribosome-associated quality control (RQC) complex marks ribosome-stalled nascent polypeptide chains for aggregation. *eLife.* 2016;5.

17. Wu Z, et al. MISTERMINATE Mechanistically Links Mitochondrial Dysfunction With Proteostasis Failure. *Molecular cell.* 2019;75(4).

18. Li S, et al. Quality-control mechanisms targeting translationally stalled and C-terminally extended poly(GR) associated with ALS/FTD. *Proc Natl Acad Sci U S A.* 2020;117(40):25104-15.

19. Rimal S, et al. Inefficient quality control of ribosome stalling during APP synthesis generates CAT-tailed species that precipitate hallmarks of Alzheimer's disease. *Acta neuropathologica communications.* 2021;9(1).

20. Wang N, and Wang D. Genome-wide transcriptome and translatome analyses reveal the role of protein extension and domestication in liver cancer oncogenesis. *Molecular genetics and genomics : MGG.* 2021;296(3).

21. Champagne J, et al. Oncogene-dependent sloppiness in mRNA translation. *Molecular cell.* 2021;81(22).

22. Rubio A, et al. Ribosome profiling reveals ribosome stalling on tryptophan codons and ribosome queuing upon oxidative stress in fission yeast. *Nucleic acids research.* 2021;49(1).

23. Dango S, et al. DNA unwinding by ASCC3 helicase is coupled to ALKBH3-dependent DNA alkylation repair and cancer cell proliferation. *Molecular cell.* 2011;44(3).

24. Gao J, et al. Suppression of ABCE1-Mediated mRNA Translation Limits N-MYC-Driven Cancer Progression. *Cancer research.* 2020;80(17).

25. Zhou X, et al. High ANKZF1 expression is associated with poor overall survival and recurrence-free survival in colon cancer. *Future oncology (London, England).* 2019;15(18).

26. Costantini S, et al. Valosin-Containing Protein (VCP)/p97: A Prognostic Biomarker and Therapeutic Target in Cancer. *International journal of molecular sciences.* 2021;22(18).

27. Bi X, et al. Drosophila caliban, a nuclear export mediator, can function as a tumor suppressor in human lung cancer cells. *Oncogene.* 2005;24(56).

28. Yang Q, and Gupta R. Zinc finger protein 598 inhibits cell survival by promoting UV-induced apoptosis. *Oncotarget.* 2017;9(5).

29. Li G, et al. ANKZF1 knockdown inhibits glioblastoma progression by promoting intramitochondrial protein aggregation through mitoRQC. *Cancer letters.* 2024.

30. Gehrke S, et al. PINK1 and Parkin control localized translation of respiratory chain component mRNAs on mitochondria outer membrane. *Cell metabolism.* 2015;21(1).

31. Forrest MD. Why cancer cells have a more hyperpolarised mitochondrial membrane

potential and emergent prospects for therapy. *bioRxiv.* 2015.

32. Shi Y, et al. Gboxin is an oxidative phosphorylation inhibitor that targets glioblastoma. *Nature.* 2019;567(7748).

33. Guièze R, et al. Mitochondrial Reprogramming Underlies Resistance to BCL-2 Inhibition in Lymphoid Malignancies. *Cancer cell.* 2019;36(4).

34. Ramamoorthy MD, et al. Reserpine Induces Apoptosis and Cell Cycle Arrest in Hormone Independent Prostate Cancer Cells through Mitochondrial Membrane Potential Failure. *Anti-cancer agents in medicinal chemistry.* 2018;18(9).

35. Heerdt BG, et al. Growth properties of colonic tumor cells are a function of the intrinsic mitochondrial membrane potential. *Cancer research.* 2006;66(3).

36. Zorova LD, et al. Mitochondrial membrane potential. *Analytical biochemistry.* 2018;552.

37. Maria A, et al. *Biochemistry, Electron Transport Chain.* StatPearls Publishing; 2020.

38. Liberti MV, and Locasale JW. The Warburg Effect: How Does it Benefit Cancer Cells? *Trends in biochemical sciences.* 2016;41(3).

39. Varn FS, et al. Glioma progression is shaped by genetic evolution and microenvironment interactions. *Cell.* 2022;185(12).

40. Rutka JT, et al. Establishment and characterization of five cell lines derived from human malignant gliomas. *Acta neuropathologica.* 1987;75(1).

41. Kim E, et al. Phosphorylation of EZH2 activates STAT3 signaling via STAT3 methylation and promotes tumorigenicity of glioblastoma stem-like cells. *Cancer cell.* 2013;23(6).

42. Sonoda Y, et al. Formation of intracranial tumors by genetically modified human astrocytes defines four pathways critical in the development of human anaplastic astrocytoma. *Cancer research.* 2001;61(13).

43. Saito S, et al. The Hbs1-Dom34 protein complex functions in non-stop mRNA decay in mammalian cells. *The Journal of biological chemistry.* 2013;288(24).

44. Chang WD, et al. Threonine-rich carboxyl-terminal extension drives aggregation of stalled polypeptides. *Molecular cell.* 2024;84(22).

45. Khan D, et al. Mechanochemical forces regulate the composition and fate of stalled nascent chains. *bioRxiv : the preprint server for biology.* 2024.

46. Morgenstern M, et al. Definition of a High-Confidence Mitochondrial Proteome at Quantitative Scale. *Cell reports.* 2017;19(13).

47. Chang YW, et al. Spatial and temporal dynamics of ATP synthase from mitochondria toward the cell surface. *Communications biology.* 2023;6(1).

48. Alavian KN, et al. An uncoupling channel within the c-subunit ring of the F1FO ATP synthase is the mitochondrial permeability transition pore. *Proceedings of the National Academy of Sciences of the United States of America.* 2014;111(29).

49. Giorgio V, et al. Dimers of mitochondrial ATP synthase form the permeability transition pore. *Proceedings of the National Academy of Sciences of the United States of America.* 2013;110(15).

50. Bonora M, et al. Role of the c subunit of the FO ATP synthase in mitochondrial permeability transition. *Cell cycle (Georgetown, Tex).* 2013;12(4).

51. Ichas F, et al. Mitochondria are excitable organelles capable of generating and conveying electrical and calcium signals. *Cell.* 1997;89(7).

52. Stockert JC, et al. Tetrazolium salts and formazan products in Cell Biology: Viability assessment, fluorescence imaging, and labeling perspectives. *Acta histochemica.* 2018;120(3).

53. Justus CR, et al. In vitro cell migration and invasion assays. *Journal of visualized experiments : JoVE*. 2014(88).

54. Grada A, et al. Research Techniques Made Simple: Analysis of Collective Cell Migration Using the Wound Healing Assay. *The Journal of investigative dermatology.* 2017;137(2).

55. Mashimo M, et al. The 89-kDa PARP1 cleavage fragment serves as a cytoplasmic PAR carrier to induce AIF-mediated apoptosis. *The Journal of biological chemistry.* 2021;296.

56. Khaket TP, et al. Ribosome stalling during c-myc translation presents actionable cancer cell vulnerability. *PNAS nexus.* 2024;3(8).

57. Comelli M, et al. F1FO ATP Synthase Is Expressed at the Surface of Embryonic Rat Heart-Derived H9c2 Cells and Is Affected by Cardiac-Like Differentiation. *Journal of cellular biochemistry.* 2016;117(2).

58. Lv L, et al. NEMF-mediated Listerin-independent mitochondrial translational surveillance by E3 ligase Pirh2 and mitochondrial protease ClpXP. *Cell reports.* 2024;43(3).

59. Cormio A, et al. Mitochondrial Caseinolytic Protease P: A Possible Novel Prognostic Marker and Therapeutic Target in Cancer. *International journal of molecular sciences.* 2021;22(12).

60. Ventura-Clapier R, et al. Transcriptional control of mitochondrial biogenesis: the central role of PGC-1alpha. *Cardiovascular research.* 2008;79(2).

61. Wu Z, et al. Mechanisms controlling mitochondrial biogenesis and respiration through the thermogenic coactivator PGC-1. *Cell*. 1999;98(1).

62. Endlicher R, et al. The Mitochondrial Permeability Transition Pore-Current Knowledge of Its Structure, Function, and Regulation, and Optimized Methods for Evaluating Its

Functional State. *Cells.* 2023;12(9).

63. Beutner G, et al. Complexes between porin, hexokinase, mitochondrial creatine kinase and adenylate translocator display properties of the permeability transition pore. Implication for regulation of permeability transition by the kinases. *Biochimica et biophysica acta.* 1998;1368(1).

64. Baines CP, et al. Voltage-dependent anion channels are dispensable for mitochondrial-dependent cell death. *Nature cell biology.* 2007;9(5).

65. Gutiérrez-Aguilar M, et al. Genetic manipulation of the cardiac mitochondrial phosphate carrier does not affect permeability transition. *Journal of molecular and cellular cardiology.* 2014;72.

66. Kokoszka JE, et al. The ADP/ATP translocator is not essential for the mitochondrial permeability transition pore. *Nature*. 2004;427(6973).

67. Karch J, et al. Inhibition of mitochondrial permeability transition by deletion of the ANT family and CypD. *Science advances.* 2019;5(8).

68. Beutner G, et al. The Mitochondrial Permeability Transition Pore and ATP Synthase. *Handbook of experimental pharmacology.* 2017;240.

69. Petronilli V, et al. Regulation of the permeability transition pore, a voltage-dependent mitochondrial channel inhibited by cyclosporin A. *Biochimica et biophysica acta.* 1994;1187(2).

70. Boyman L, et al. Dynamics of the mitochondrial permeability transition pore: Transient and permanent opening events. *Archives of biochemistry and biophysics.* 2019;666.

71. Antoniel M, et al. The unique histidine in OSCP subunit of F-ATP synthase mediates inhibition of the permeability transition pore by acidic pH. *EMBO reports.* 2018;19(2).

72. Carraro M, et al. The Unique Cysteine of F-ATP Synthase OSCP Subunit Participates in Modulation of the Permeability Transition Pore. *Cell reports.* 2020;32(9).

73. Wang L, et al. A Multisite-Binding Switchable Fluorescent Probe for Monitoring Mitochondrial ATP Level Fluctuation in Live Cells. *Angewandte Chemie (International ed in English).* 2016;55(5).

Figure Legends

Figure 1. Evidence for msiCAT-tailing on mitochondrial proteins in GBM cells

(A) RQC gene expression levels in GBM tumor tissues (n=153) compared to normal brain tissues (n=206) (unpaired Student's t-test; *, logFC (fold change)>1; adj.P.Val<0.001). (B) Western blot analysis of msiCAT-tailed mitochondrial proteins and RQC factors in patient-derived GSC and control NSC cells, using ACTIN as the loading control. Red arrowheads indicate short CAT-tailed mitochondrial proteins; "short" and "long" refer to exposure time; the red numbers represent fold changes compared to controls (NSC). (C) Western blot of 5×FLAG-tagged β-globin reporter proteins in GBM and control cells, showing more CAT-tailed proteins in GBM cells, using ACTIN as the loading control. The red numbers represent fold changes compared to controls (NHA without any treatment); the purple numbers represent the ratio of red (CAT-tailed) to green (non-CAT-tailed) sections. (D) Western blot of overexpressed ATP5α-AT3 and ATP5α-AT20 in GBM and control cells, using GAPDH as the loading control; arrowheads indicate endogenous ATP5α, ATP5α-AT3, ATP5α-AT20, and oligomers/aggregates of msiCAT-tailed ATP5α proteins. The purple numbers represent the ratio of red (exogenous) to green (endogenous) sections. (E) Immunofluorescence staining shows endogenous ATP5α protein aggregates in GBM cells, with TOM20 (red) as a mitochondrial marker. White arrows indicate ATP5α protein aggregates. (F) Quantification of E (n=3; chi-squared test; ***, $P < 0.001$; ****, $P < 0.0001$); the total number of cells counted is indicated in the columns.

Figure 2. Impact of msiCAT-tailed ATP5α proteins on mitochondrial functions in GBM cells

(A) TMRM staining shows a high mitochondrial membrane potential in patient-derived GSC cells (n=3; unpaired Student's t-test; ***, $P < 0.001$; ****, $P < 0.0001$). (B) ATP measurement shows a low mitochondrial ATP production in patient-derived GSC cells (n=3; unpaired Student's t-test; **, $P < 0.01$; ***, $P < 0.001$). (C, D) JC-10 staining reveals a reduced mitochondrial membrane potential in GBM cells, but not in NHA control cells, upon both genetic (C) and pharmacological (D) inhibition of the msiCAT-tailing pathway (n=3; unpaired Student's t-test; ***, $P < 0.001$; ****, $P < 0.0001$; ns, not significant). (E) JC-10 staining reveals an increased mitochondrial membrane potential in GBM cells, but not in control cells, upon overexpression of ATP5□-AT3 and ATP5□-AT20 (n=3; unpaired Student's t-test; ****, $P < 0.0001$; ns, not significant). (F) Western blot of FLAG-tagged ATP5□, NEMF, and ANKZF1 in GBM cells and control cells, using ACTIN as the loading control. (G) JC-10 staining reveals an increased mitochondrial membrane potential in GBM cells, but not in NHA control cells, upon overexpression of ATP5□-AT3 and ATP5□-AT20 with concurrent genetic inhibition of the endogenous msiCAT-tailing pathway (n=3; unpaired Student's t-test; *, $P < 0.05$; **, $P < 0.01$). (H) BN-PAGE western blot of ATP5□ and Flag shows that ATP5□-AT3 is incorporated into the mitochondrial Complex-V (ATP synthase), while ATP5□-AT20 forms high molecular weight protein aggregates in GBM cells. SC: respiratory supercomplex; C-V: Complex-V/ATP synthase. (I, K) Oxygen consumption rate (OCR) data indicate a reduction in mitochondrial oxygen consumption in SF268 cells expressing ATP5□-AT3 and ATP5□-AT20. Oligomycin (1.5 μM), FCCP (1.0 μM), and rotenone/antimycin A (R/A, 0.5 μM) were sequentially added. (J, L) Statistics of mitochondrial respiration parameters in (I, K), including non-mitochondrial respiration, basal respiration, maximum respiration, spare respiration, proton leaks, and ATP

production (n=3; unpaired Student's t-test; *, $P < 0.05$; **, $P < 0.01$; ***, $P < 0.001$; ****, $P < 0.0001$; ns, not significant).

Figure 3. **msiCAT-tailing product regulates MPTP status in GBM cells**

(A, C) MPTP activity assay shows reduced mitochondrial permeability transition pore opening in GSC cells compared to NHA (control) cells. Pharmacological (A, anisomycin 200 nM) and genetic (sgNEMF) inhibition of CAT-tailing reverse it. (B, D) Quantification of (A, C) (n=3; unpaired Student's t-test; ****, $P < 0.0001$; ns, not significant). (E, G) Immunofluorescence staining shows that anisomycin treatment (E) and sgNEMF (G) inhibit endogenous ATP5α protein aggregation in GBM cells, using TOM20 (red) as a mitochondrial marker. (F, H) Quantification of (E, G) (n=3; chi-squared test; *, $P < 0.05$; **, $P < 0.01$; ***, $P < 0.001$); the total number of cells counted is indicated in the columns. (I) Calcium retention capacity (CRC) assay of isolated mitochondria, measured with Calcium Green-5N dye, shows high CRC in GBM cells compared to control NHA cells. CsA (Cyclosporin A, MPTP inhibitor) serves as a positive control. (J) Statistic of (I) shows attenuated CRC in mitochondria pretreated with anisomycin or with sgNEMF (n=10; unpaired Student's t-test; ***, $P < 0.001$; ****, $P < 0.0001$). (K) MPTP activity assay shows that ectopic expression of ATP5α-AT3 and ATP5α-AT20 inhibits MPTP opening in GBM cells. (L) Quantification of (K) (n=3; unpaired Student's t-test; ****, $P < 0.0001$). (M) BN-PAGE western blot shows that ATP5α-AT3 and ATP5α-AT20 expression alters ANT1/2 protein patterns in GBM cells, resulting in a missing band (circled in yellow dashed line), and formation of high molecular weight aggregates. SC: respiratory supercomplex; C-V: Complex V/ATP synthase.

Figure 4. msiCAT-tailed ATP5□ protein promotes GBM progression

(A) MTT assay indicates increased proliferation caused by ATP5□-AT3 and ATP5□-AT20 expression in GBM cells (n=3; unpaired Student's t-test; **, $P < 0.01$; ***, $P < 0.001$). (B) MTT assay indicates no change in proliferation caused by ATP5□-AT3 and ATP5□-AT20 expression in NHA cells (n=3; unpaired Student's t-test; ns, not significant). (C) Transwell assay reveals enhanced migration induced by ATP5□-AT3 and ATP5□-AT20 expression in GBM (SF) cells but not in control (NHA) cells. (D) Quantification of (C) shows the number of migrated cells (n=3; unpaired Student's t-test; ***, $P < 0.001$; ns, not significant). (E) MTT assay indicates an increased proliferation in GBM cells, upon overexpression of ATP5□-AT3 and ATP5-AT20 with concurrent genetic inhibition of the endogenous msiCAT-tailing pathway (n=3; unpaired Student's t-test; *, $P < 0.05$; **, $P < 0.01$). (F) Transwell assay reveals enhanced migration upon overexpression of ATP5□-AT3 and ATP5□-AT20 with concurrent genetic inhibition of the endogenous msiCAT-tailing pathway. (G) Quantification of (F) shows the number of migrated cells (n=3; unpaired Student's t-test; ***, $P < 0.001$; ****, $P < 0.0001$). (H) TUNEL staining shows that staurosporine (STS, 1 μM)-induced apoptosis is attenuated by ATP5□-AT3 and ATP5□-AT20 expression in GBM cells, using TUNEL-Cy3 as an apoptotic cell indicator and DAPI as a nucleus indicator. (I) Quantification of (H) shows the percentage of TUNEL-positive cells in the population (n=3; unpaired student's t-test; ***, $P < 0.001$), using DMSO as the vehicle control. (J) MTT assay indicates an enhanced resistance to temozolomide (TMZ, 150 μM) induced by ATP5□-AT3 and ATP5□-AT20 expression. The TMZ-treated/SF-Ctrl group is used as the control (n=3; unpaired Student's t-test; ***, $P < 0.001$).

Figure 5. Inhibition of msiCAT-tailing impedes GBM progression

(A) Cell viability assay shows greater sensitivity to anisomycin treatment in patient-derived GSC cells than control NSC cells at 48 hours (n=3; unpaired Student's t-test; **, $P < 0.001$; ****, $P < 0.0001$; compared to controls at the corresponding dose). (B) MTT assay indicates reduced GBM cell proliferation by genetic inhibition of the msiCAT-tailing pathway (n=3; unpaired Student's t-test; **, $P < 0.01$; ***, $P < 0.001$; ****, $P < 0.0001$, compared to controls at the corresponding time). (C) MTT assay indicates reduced NHA cell proliferation by genetic inhibition of the msiCAT-tailing pathway (n=3; unpaired Student's t-test; **, $P < 0.01$; ****, $P < 0.0001$, compared to controls at the corresponding time). (D, F) Transwell assay reveals that both genetic (D) and pharmacological (F) inhibition of the msiCAT-tailing pathway hampers the migration of GBM cells but not control cells. (E, G) Quantification of (D, F) showing the number of migrated cells (n=3; unpaired Student's t-test; ***, $P < 0.001$; ****, $P < 0.0001$; ns, not significant). (H, J) TUNEL staining shows that both genetic (H) and pharmacological (J) inhibition of the msiCAT-tailing pathway enhances STS-induced apoptosis in GBM cells, using TUNEL-Cy3 as an apoptotic cell indicator and DAPI as a nucleus indicator. (I, K) Quantification of (H, J) showing the percentage of TUNEL-positive cells in the population (n=3; unpaired Student's t-test; **** $P < 0.0001$), using DMSO as the vehicle control. (L) MTT assay shows that pharmacological inhibition of the msiCAT-tailing pathway decrease the resistance of GBM cells to temozolomide (TMZ, 150 μM) treatment (n=3; unpaired Student's t-test; * $P < 0.05$; **, $P < 0.01$). (M) Neurosphere formation assay shows that reduced spheroid formation caused by pharmacological inhibition of the msiCAT-tailing pathway can synergize with TMZ in GBM cells. (N) Quantification of (M) (n=3; unpaired Student's t-test; **, $P < 0.01$).

Figure 6. Impact of msiCAT-tail modified ATP5α protein on mitochondrial function in GBM cells

In healthy cells, ATP5α protein, encoded by the nuclear genome, is imported into the mitochondrial matrix via the TOM/TIM complex through co-translational import and incorporated into ATP synthase (Left). Conversely, in GBM cells, the CAT-tailed ATP5α protein can either form aggregates near the mitochondrial outer membrane or be imported into the mitochondria. Within the mitochondrial matrix, proteins with shorter CAT-tails readily integrate into ATP synthase, disrupting its functionality. This dysfunction is characterized by a reduced ATP synthesis rate and proton (H^+) accumulation, leading to an elevated mitochondrial membrane potential ($\Delta\Psi m$). These alterations in ATP synthase ultimately trigger malfunction of the MPTP, consequently affecting cell proliferation, migration, and resistance to drug-induced apoptosis (Right).

Supplementary Figure and Table Legends

Figure S1. RQC pathway activity in GBM cells

(A) Immunofluorescence staining shows elevated NEMF and reduced ANKZF1 endogenous protein levels in the tumor tissue of the GBM mouse model compared to wild-type brain tissue. Tumor identification is indicated by GFP (green). (B) Quantification of A (n=3; unpaired Student's t-test; ****, $P < 0.0001$). (C) Western blot analysis of select RQC factors in control cell lines (SVG, NHA) and GBM cell lines (SF268, GSC827), using ACTIN as the loading control. Red numbers represent fold changes in protein levels relative to controls (SVG).

Figure S2. AT repeat sequences mimicking CAT-tails induce protein aggregates in cells

(A) Western blot analysis of ATP5α in GSC cells, using GAPDH as the loading control. The red arrowhead indicates the modified ATP5α form; “short” and “long” refer to exposure time. (B) Western blot analysis of Flag-tagged ATP5α in GSC and control cells, using ACTIN as the loading control. The red arrowhead indicates the modified Flag-ATP5α form. (C) Immunofluorescence staining shows that Flag-tagged ATP5α-AT3 and ATP5α-AT20 (green) form aggregates in GBM and control cells, using TOM20 (red) as a mitochondrial marker. (D) Quantification of C (n=3; chi-squared test; ***, $P < 0.001$; ****, $P < 0.0001$); the total number of cells counted is indicated in the columns. (E) Western blot of Flag-tagged ATP5α-GS3 and ATP5α-GS20 in GBM cells, using ACTIN as the loading control. (F) Immunofluorescence staining shows that Flag-tagged ATP5α-GS3 and ATP5α-GS20 (green) do not form aggregates in GBM cells, using TOM20 (red) as a mitochondrial marker. (G) Quantification of F (n=3; chi-squared test; ns, not significant); the total number of cells counted is indicated in the columns.

Figure S3. Aggregation of CAT-tailed mitochondrial proteins observed *in vivo*

(A) Immunofluorescence staining shows that endogenous NDUS3 protein aggregates in GBM cells, with TOM20 (red) as a mitochondrial marker. White arrows indicate NUDS3 protein aggregates. (B) Quantification of A (n=3; chi-squared test; *, $P < 0.05$); the total number of cells counted is indicated in the columns. (C) Immunofluorescence staining shows that endogenous ATP5 protein forms aggregates in the tumor tissue from the GBM mouse model but not in the wild-type brain tissue, using TOM20 (blue) as a mitochondrial marker. Tumor identification is indicated by GFP (green). White arrowheads indicate ATP5 (red) aggregates. Yellow lines indicate the regions selected for intensity analysis in (D). (D) Fluorescence intensity profiles show ATP5 (red) and TOM20 (blue) signals in wild-type and tumor tissues. Black arrows indicate ATP5 aggregates located outside of mitochondria. (E) Quantification of C (n=3; chi-squared test; ****, $P < 0.0001$); the total number of cells counted is indicated in the columns.

Figure S4. Aberrant mitochondrial function in GBM cells

(A) JC-10 staining reveals elevated mitochondrial membrane potentials in GBM cells compared to NHA (control) cells (n=3; unpaired Student's t-test; ***, $P < 0.001$). (B) Analysis with BioTracker ATP red dye staining shows reduced mitochondrial ATP production in GBM cells compared to NHA (control) cells, using MitoTracker Green as the mitochondrial mass indicator for normalization. (C) Quantification of (B) (n=3; unpaired Student's t-test; ****, $P < 0.0001$). (D) Western blot of NEMF and ANKZF1 in GBM and control cells, confirming the successful overexpression and knockdown of target proteins, using ACTIN as the loading control. (E) JC-10 staining reveals no change of mitochondrial membrane potential in GBM cells, upon

overexpression of ATP5□-GS3 and ATP5□-GS20 (n=3; unpaired Student's t-test; ****, $P < 0.0001$; ns, not significant).

Figure S5. Cycloheximide does not impact mitochondrial functions

(A) MPTP activity assay shows that MPTP opening is not affected by the cycloheximide treatment (100 μg/mL) in cells. (B) Quantification of (A) (n=3; unpaired Student's t-test; ns, not significant). (C) Immunofluorescence staining shows no inhibition of endogenous ATP5□ protein aggregation by cycloheximide (100 μg/mL) treatment in GBM cells, using TOM20 (red) as a mitochondrial marker. (D) Quantification of (C) (n=3; chi-squared test; ns, not significant); the total number of cells counted is indicated in the columns. (E) MPTP activity assay reveals the increased Calcien signal in GBM cells, upon overexpression of ATP5□-AT3 and ATP5□-AT20 with concurrent genetic inhibition of the msiCAT-tailing pathway (n=3; unpaired Student's t-test; **, $P < 0.01$; ***, $P < 0.001$; ****, $P < 0.0001$).

Figure S6. The CAT-tailed ATP5□ variant has no interaction with MPTP proteins

(A) Calcium retention capacity (CRC) assay of isolated mitochondria, measured with Calcium Green-5N dye, upon cycloheximide (100 μg/mL) treatment and CAT-tailing enhancement (oeNEMF and siANKZF1). (B) Statistic of (A) shows changes in CRC in GBM cells or control cells (n=10; unpaired Student's t-test; **, $P < 0.01$; ***, $P < 0.001$). (C) Co-immunoprecipitation data show no direct interaction between ATP5□ and either CypD or ANT1/2 can be found in GBM cells. Red arrowheads indicate target proteins. (D) Western blotting of cytosolic and

isolated mitochondrial fractions shows ATP5□-AT3 expression reduces CypD levels in GBM cells, using TOM20 as a mitochondrial marker and loading control.

Figure S7. Effect of GS repeat tails on GBM proliferation and migration

(A) MTT assay indicates no significant change in GBM proliferation upon ATP5□-GS3 and ATP5□-GS20 expression (n=3; unpaired Student's t-test; **, $P < 0.01$; ns, not significant). (B) Wound healing assay reveals promoted GBM migration upon ATP5□-AT3 and ATP5□-AT20 expression. (C) Quantification of (B) shows an increased healing rate, indicated by scratch wound coverage at both 24 and 48 hours (n=3; unpaired Student's t-test; **, $P < 0.01$). (D) Transwell assay reveals no significant alteration in GBM migration upon ATP5□-GS3 and ATP5□-GS20 expression. (E) Quantification of (D) shows the number of migrated cells (n=3; unpaired Student's t-test; ns, not significant). (F) RT-PCR shows no increase in mRNA levels of mitochondrial unfolded protein response genes, using ACTB as the control.

Figure S8. GBM cells exhibit increased resistance to apoptosis

(A) TUNEL staining shows that GBM cells are more resistant to staurosporine (STS, 1 μM)-induced apoptosis compared to control cells, using TUNEL-Cy3 as an apoptotic cell indicator and DAPI as a nucleus indicator. (B) Quantification of A shows the percentage of TUNEL-positive cells in the population (n=3; unpaired Student's t-test; ***, $P < 0.0001$; ****, $P < 0.0001$), using DMSO as the vehicle control. (C) Western blot analysis of PARP shows that GBM cells are more resilient against STS-induced apoptosis at 30-, 90-, and 180-min post-treatment. Cleaved PARP is used as an apoptosis marker. ACTIN and GAPDH are used as loading controls. Red numbers below each blot represent the ratios of cleaved PARP (c-PARP) to total PARP

protein. (D, F) Flow cytometry analysis using Annexin V-FITC/Propidium Iodide (PI) staining shows alterations in apoptosis rates in GBM cells upon ATP5□-AT3, ATP5□-AT20, ATP5□-GS3, and ATP5□-GS20 expression. The apoptotic cell population (Annexin V positive, PI negative) is represented in the fourth quadrant (right lower). (E, G) Quantification of (D, F) shows the percentages of apoptotic cells (n=3; unpaired Student's t-test; **, $P < 0.001$; ***, $P < 0.0001$).

Figure S9. No effect of Cycloheximide on GBM apoptosis response

(A) Caspase-3/7 activity assay shows increased apoptosis in GBM cells caused by anisomycin treatment (n=3; unpaired Student's t-test; ***, $P < 0.001$; ****, $P < 0.0001$; compared to the control group (DMSO) at the corresponding time). (B, C) Western blot analysis of PARP in anisomycin-treated and cycloheximide-treated GSC cells indicates that pharmacological inhibition of the msiCAT-tailing pathway enhances STS-induced apoptosis, using ACTIN as a loading control. Red numbers below each blot represent the ratios of cleaved PARP (c-PARP) to total PARP protein. (D, F) Flow cytometry analysis using Annexin V-FITC/Propidium Iodide (PI) staining shows alterations in apoptosis rates in GBM cells upon genetic (D) and pharmacological (F) inhibition of the msiCAT-tailing pathway. The apoptotic cell population (Annexin V positive, PI negative) is represented in the fourth quadrant (right lower). (E, G) Quantification of (D, F) shows the percentages of apoptotic cells (n=3; unpaired Student's t-test; **, $P < 0.01$; ***, $P < 0.001$; ****, $P < 0.0001$; ns, not significant).

Table S1. Differential expression analysis of RQC genes in GBM patients compared to healthy controls

Figure 1

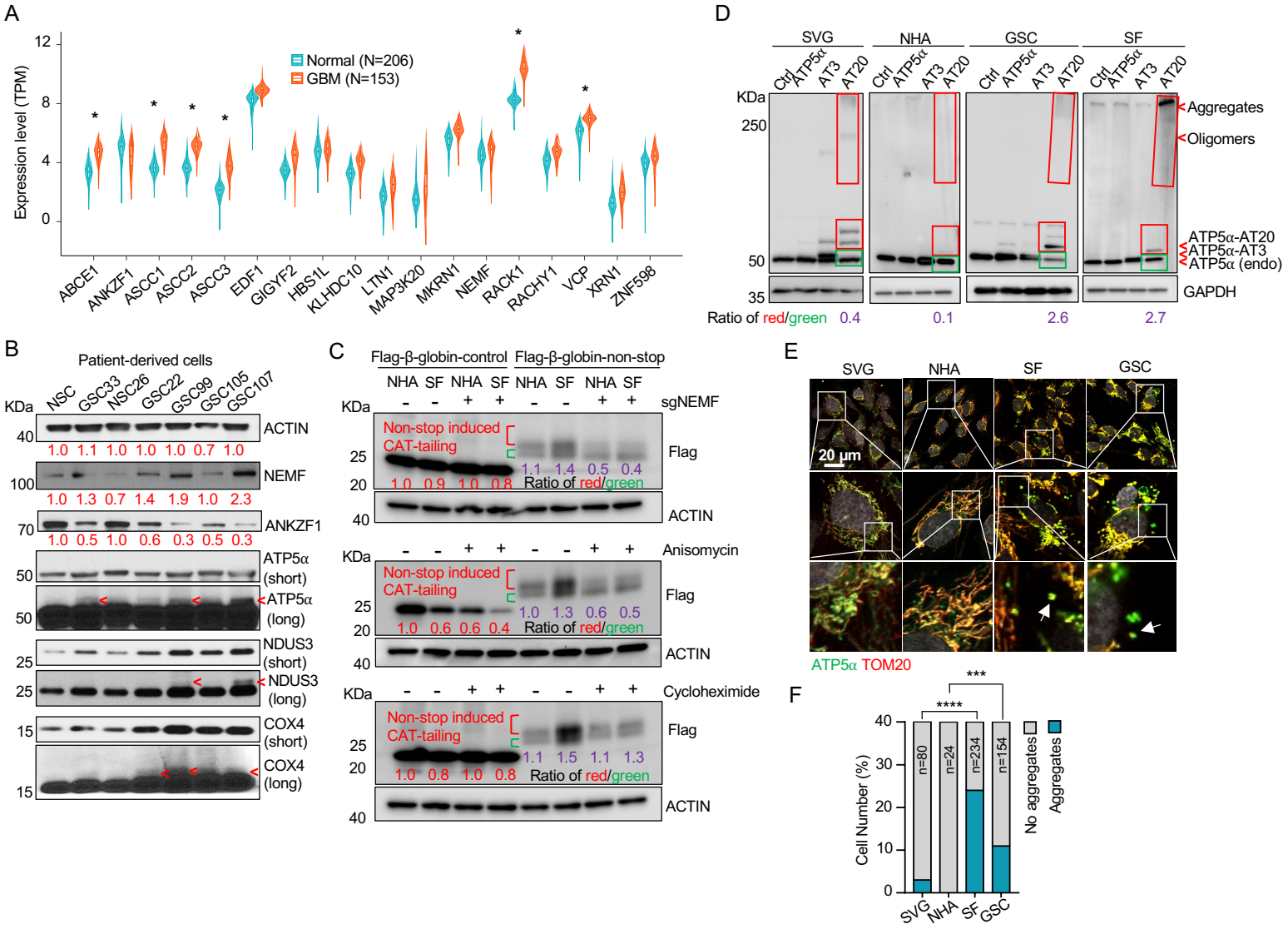
A
Expression level (TPM)
Normal (N=206)
GBM (N=153)
ABCE1
ANKZF1
ASCC1
ASCC2
ASCC3
EDF1
GIGYF2
HBS1L
KLHDC10
LTN1
MAP3K20
MKRN1
NEMF
RACK1
RACHY1
VCP
XRN1
ZNF598
B
Patient-derived cells
NSC
GSC33
NSC26
GSC22
GSC99
GSC105
GSC107
ACTIN
NEMF
ANKZF1
ATP5α (short)
ATP5α (long)
NDUS3 (short)
NDUS3 (long)
COX4 (short)
COX4 (long)
C
Flag-β-globin-control
Flag-β-globin-non-stop
sgNEMF
Anisomycin
Cycloheximide
Non-stop induced CAT-tailing
Flag
ACTIN
Ratio of red/green
D
SVG
NHA
GSC
SF
Ctrl
ATP5α
AT3
AT20
Aggregates
Oligomers
ATP5α-AT20
ATP5α-AT3
ATP5α (endo)
GAPDH
Ratio of red/green
E
20 μm
ATP5α TOM20
F
Cell Number (%)
No aggregates
Aggregates
n=80
n=24
n=234
n=154

Figure 2

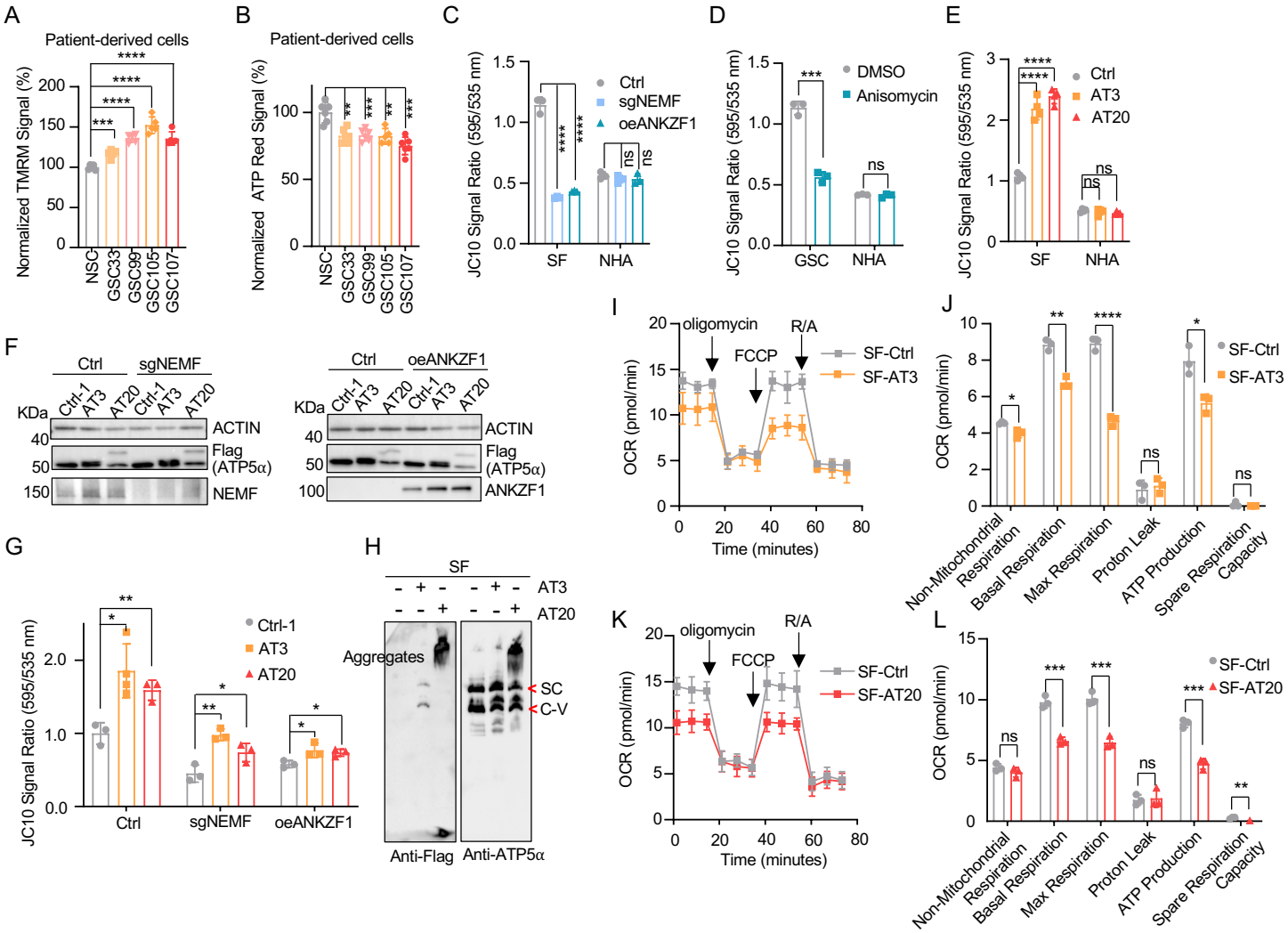
A
Patient-derived cells
Normalized TMRM Signal (%)
NSC
GSC33
GSC99
GSC105
GSC107
B
Patient-derived cells
Normalized ATP Red Signal (%)
C
JC10 Signal Ratio (595/535 nm)
Ctrl
sgNEMF
oeANKZF1
SF
NHA
D
JC10 Signal Ratio (595/535 nm)
DMSO
Anisomycin
GSC
NHA
E
JC10 Signal Ratio (595/535 nm)
Ctrl
AT3
AT20
SF
NHA
F
Ctrl
sgNEMF
Ctrl-1
AT3
AT20
KDa
ACTIN
Flag (ATP5α)
NEMF
oeANKZF1
ANKZF1
G
JC10 Signal Ratio (595/535 nm)
Ctrl-1
AT3
AT20
Ctrl
sgNEMF
oeANKZF1
H
SF
AT3
AT20
Aggregates
SC
C-V
Anti-Flag
Anti-ATP5α
I
oligomycin
FCCP
R/A
SF-Ctrl
SF-AT3
OCR (pmol/min)
Time (minutes)
J
SF-Ctrl
SF-AT3
OCR (pmol/min)
Non-Mitochondrial Respiration
Basal Respiration
Max Respiration
Proton Leak
ATP Production
Spare Respiration Capacity
K
oligomycin
FCCP
R/A
SF-Ctrl
SF-AT20
OCR (pmol/min)
Time (minutes)
L
SF-Ctrl
SF-AT20
OCR (pmol/min)
Non-Mitochondrial Respiration
Basal Respiration
Max Respiration
Proton Leak
ATP Production
Spare Respiration Capacity

Figure 3

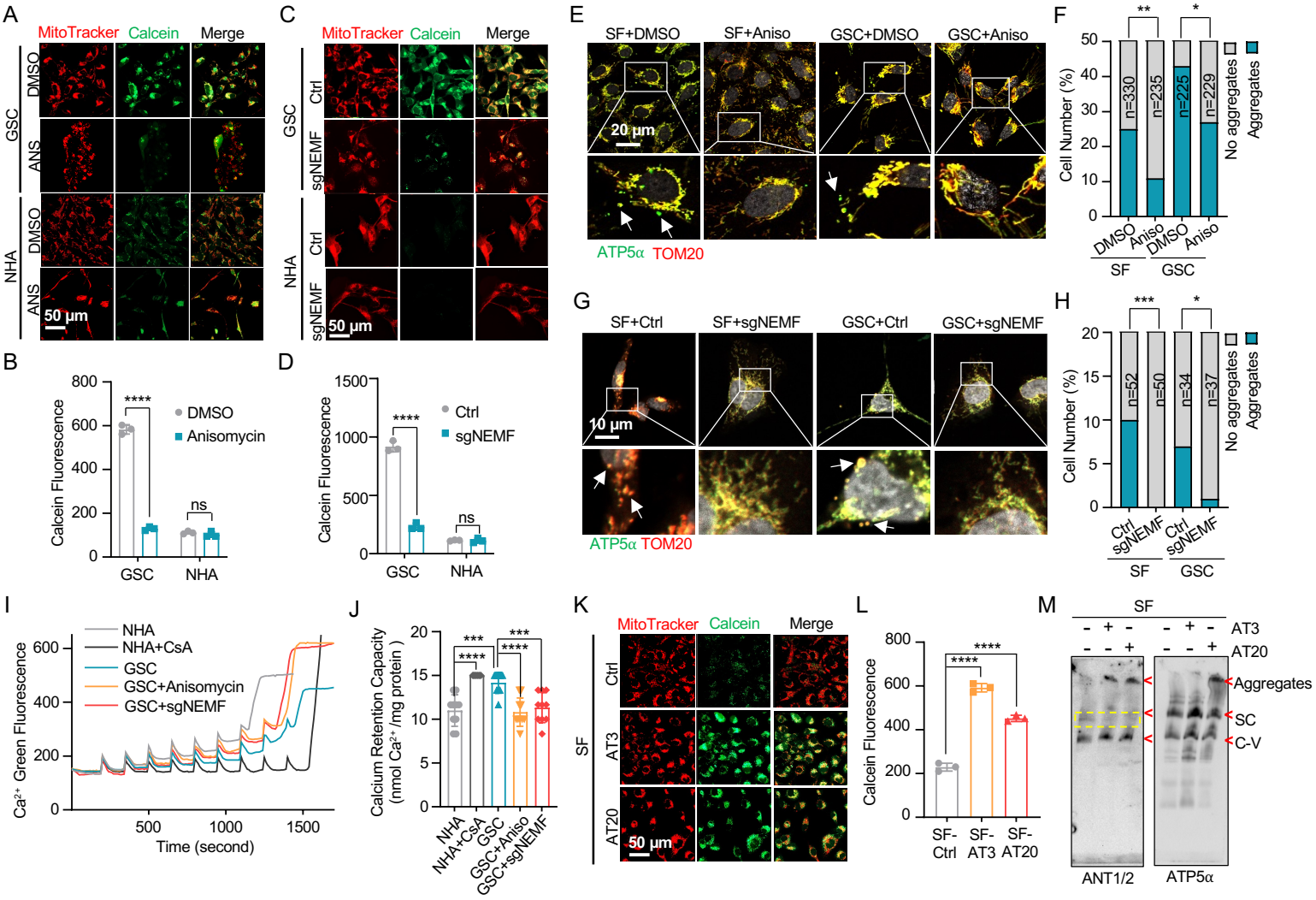
A
MitoTracker
Calcein
Merge
GSC
DMSO
ANIS
NHA
DMSO
ANIS
50 μm
B
Calcein Fluorescence
DMSO
Anisomycin
****
ns
GSC
NHA
C
MitoTracker
Calcein
Merge
GSC
Ctrl
sgNEMF
NHA
Ctrl
sgNEMF
50 μm
D
Calcein Fluorescence
Ctrl
sgNEMF
****
ns
GSC
NHA
E
SF+DMSO
SF+Aniso
GSC+DMSO
GSC+Aniso
20 μm
ATP5α
TOM20
F
Cell Number (%)
No aggregates
Aggregates
n=330
n=235
n=225
n=229
**
*
DMSO
Aniso
DMSO
Aniso
SF
GSC
G
SF+Ctrl
SF+sgNEMF
GSC+Ctrl
GSC+sgNEMF
10 μm
ATP5α
TOM20
H
Cell Number (%)
No aggregates
Aggregates
n=52
n=50
n=34
n=37
***
*
Ctrl
sgNEMF
Ctrl
sgNEMF
SF
GSC
I
NHA
NHA+CsA
GSC
GSC+Anisomycin
GSC+sgNEMF
Ca2+ Green Fluorescence
Time (second)
J
Calcium Retention Capacity
(nmol Ca2+/mg protein)
***
****
***
****
NHA
NHA+CsA
GSC
GSC+Aniso
GSC+sgNEMF
K
MitoTracker
Calcein
Merge
SF
Ctrl
AT3
AT20
50 μm
L
Calcein Fluorescence
****
****
SF-Ctrl
SF-AT3
SF-AT20
M
SF
AT3
AT20
Aggregates
SC
C-V
ANT1/2
ATP5α

Figure 4

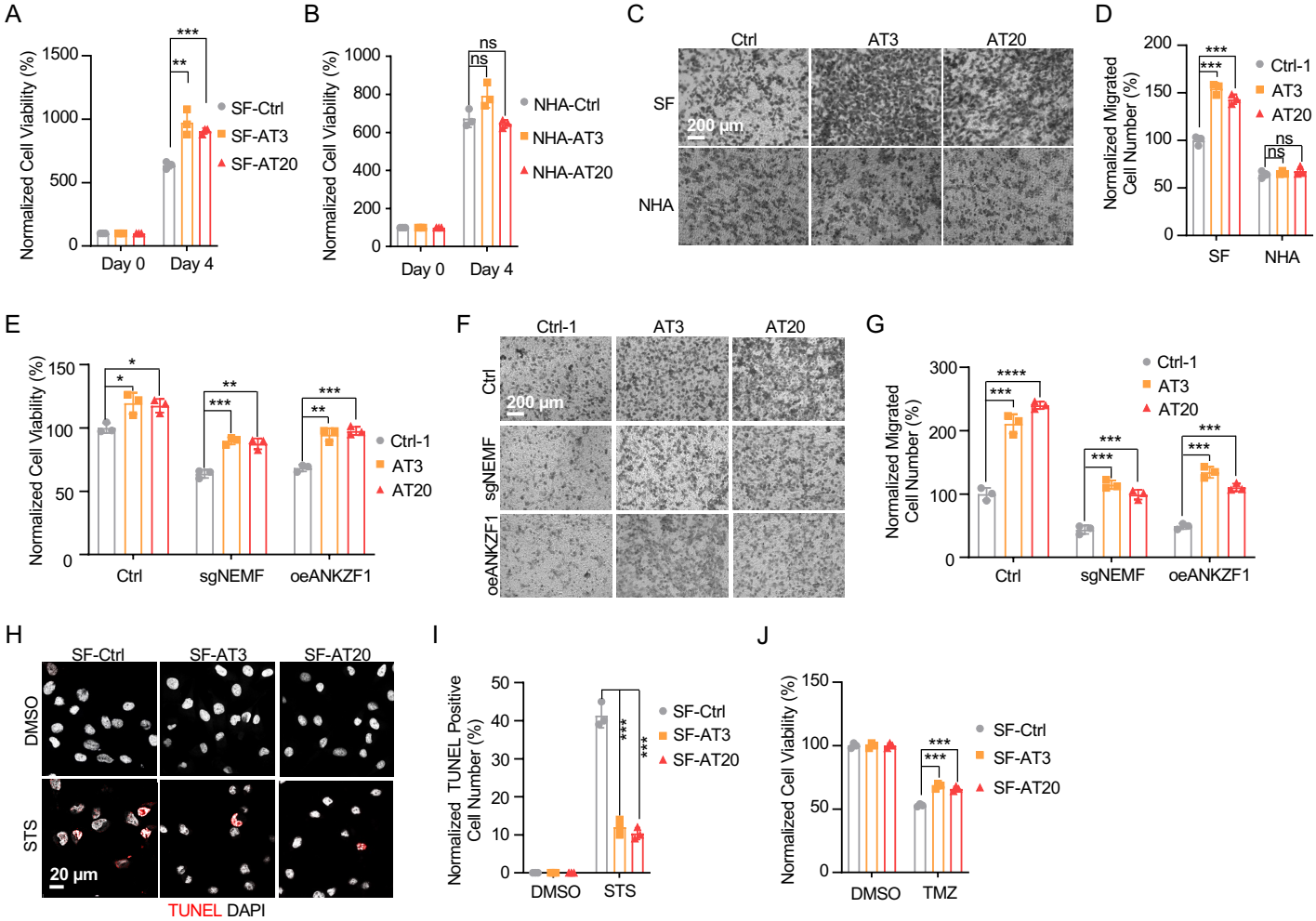
A
Normalized Cell Viability (%)
1500
1000
500
0
Day 0
Day 4
***
**
SF-Ctrl
SF-AT3
SF-AT20
B
Normalized Cell Viability (%)
1000
800
600
400
200
0
Day 0
Day 4
ns
ns
NHA-Ctrl
NHA-AT3
NHA-AT20
C
Ctrl
AT3
AT20
SF
NHA
200 μm
D
Normalized Migrated Cell Number (%)
200
150
100
50
0
SF
NHA
***
***
ns
ns
Ctrl-1
AT3
AT20
E
Normalized Cell Viability (%)
150
100
50
0
Ctrl
sgNEMF
oeANKZF1
*
*
**
***
***
**
Ctrl-1
AT3
AT20
F
Ctrl-1
AT3
AT20
Ctrl
sgNEMF
oeANKZF1
200 μm
G
Normalized Migrated Cell Number (%)
300
200
100
0
Ctrl
sgNEMF
oeANKZF1
****
***
***
***
***
***
Ctrl-1
AT3
AT20
H
SF-Ctrl
SF-AT3
SF-AT20
DMSO
STS
20 μm
TUNEL DAPI
I
Normalized TUNEL Positive Cell Number (%)
50
40
30
20
10
0
DMSO
STS
***
***
SF-Ctrl
SF-AT3
SF-AT20
J
Normalized Cell Viability (%)
150
100
50
0
DMSO
TMZ
***
***
SF-Ctrl
SF-AT3
SF-AT20

Figure 5

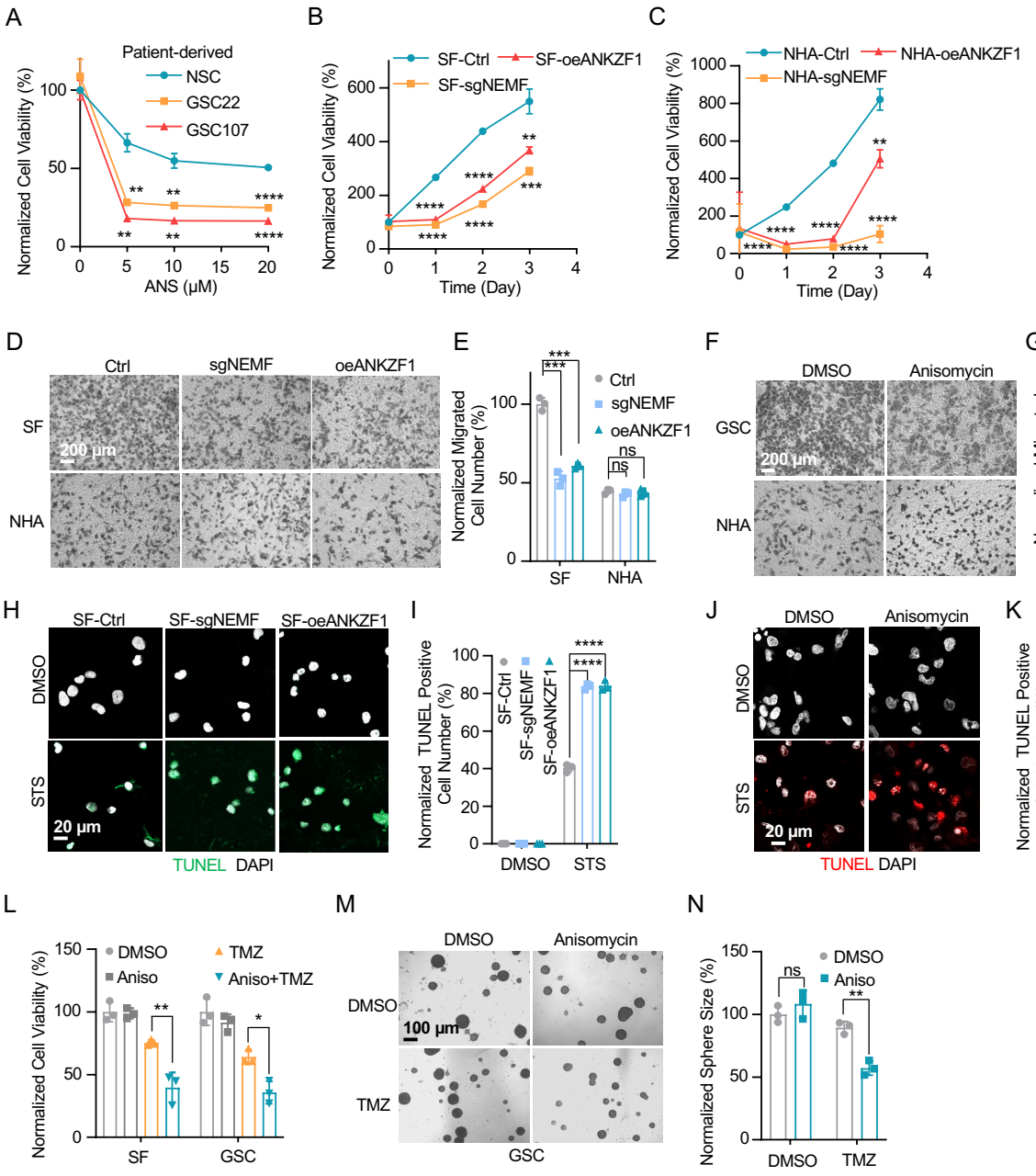
A
Patient-derived
NSC
GSC22
GSC107
Normalized Cell Viability (%)
ANS (μM)
B
SF-Ctrl
SF-oeANKZF1
SF-sgNEMF
Normalized Cell Viability (%)
Time (Day)
C
NHA-Ctrl
NHA-oeANKZF1
NHA-sgNEMF
Normalized Cell Viability (%)
Time (Day)
D
Ctrl
sgNEMF
oeANKZF1
SF
NHA
200 μm
E
Ctrl
sgNEMF
oeANKZF1
Normalized Migrated Cell Number (%)
SF
NHA
ns
F
DMSO
Anisomycin
GSC
NHA
200 μm
G
DMSO
Aniso
Normalized Migrated Cell Number (%)
GSC
NHA
ns
H
SF-Ctrl
SF-sgNEMF
SF-oeANKZF1
DMSO
STS
20 μm
TUNEL DAPI
I
SF-Ctrl
SF-sgNEMF
SF-oeANKZF1
Normalized TUNEL Positive Cell Number (%)
DMSO
STS
J
DMSO
Anisomycin
DMSO
STS
20 μm
TUNEL DAPI
K
DMSO
Aniso
Normalized TUNEL Positive Cell Number (%)
DMSO
STS
L
DMSO
Aniso
TMZ
Aniso+TMZ
Normalized Cell Viability (%)
SF
GSC
M
DMSO
Anisomycin
DMSO
TMZ
100 μm
GSC
N
DMSO
Aniso
Normalized Sphere Size (%)
ns
DMSO
TMZ

Figure 6

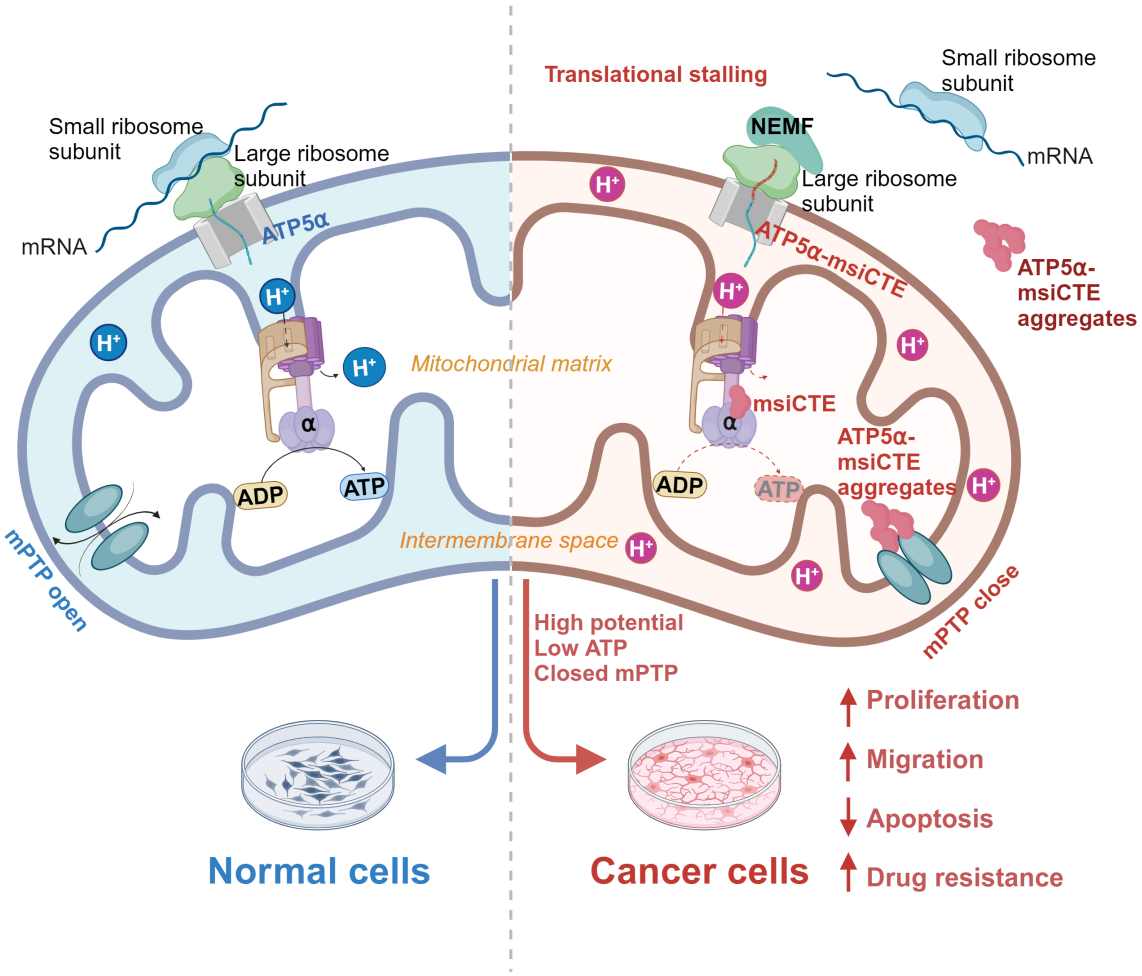

Created with BioRender.com by Bei Zhang